The Novel Role of Midbody-Associated mRNAs in Regulating Abscission

Trey Farmer[1,4], Katherine F. Vaeth[1,4], Ke-Jun Han[1], Raeann Goering[2], J. Matthew Taliaferro[2,3,5], and Rytis Prekeris[1,5]

1. Department of Cell and Developmental Biology, University of Colorado Anschutz Medical Campus, Aurora, CO, 80045
2. Department of Biochemistry and Molecular Genetics, University of Colorado Anschutz Medical Campus, Aurora, CO, 80045
3. RNA Bioscience Initiative, University of Colorado Anschutz Medical Campus, Aurora, CO, 80045
4. These authors contributed equally to this work and are listed alphabetically
5. Corresponding authors: matthew.taliaferro@cuanschutz.edu; rytis.prekeris@cuanschutz.edu

Abstract

Midbodies (MBs) have been shown to function during telophase as a recruiting hub, especially for ESCRT-III complex subunits, to regulate the abscission step of cytokinesis. However, the molecular machinery governing specific protein targeting and activation at the MB remains poorly understood. Until recently, it was thought that abscission regulating proteins, such as ESCRT-III complex subunits, accumulate at the MB by directly or indirectly binding to the MB resident protein, CEP55. However, recent studies have shown that depletion of CEP55 does not fully block ESCRT-III targeting to the MB, and cells in CEP55 knock-out mice divide normally. Additionally, since MBs are microtubule-rich, proteinaceous structures, it is conceptually hard to imagine how large protein complexes, such as the ESCRT-III complex, can successfully diffuse into the MB from the cytosol in a rapid and highly regulated manner. Here, we show that MBs contain mRNAs and that these MB-associated mRNAs can be locally translated, resulting in the accumulation of abscission-regulating proteins. We also demonstrate that localized MB-associated translation of CHMP4B is required for its targeting to the abscission site and that 3′ UTR-dependent CHMP4B mRNA targeting to the MB is required for successful completion of cytokinesis. Finally, we identify regulatory *cis*-elements within RNAs that are necessary and sufficient for mRNA trafficking to the MB. Based on all this data, we propose a novel method of regulating cytokinesis and abscission by MB-associated targeting and localized translation of selective mRNAs.

Introduction

The cell cycle is a key event during the development, growth, and reproduction of all organisms. Cytokinesis is the final stage of the cell cycle that results in the physical separation of two daughter cells. The mother cell divides by the formation of the cleavage furrow, leaving two daughter cells connected by a microtubule-rich intercellular bridge. Additionally, during ingression of the cleavage furrow, the central spindle microtubules are compacted to form a structure known as the midbody (MB). To complete cytokinesis, the intercellular bridge must be cleaved on one or both sides of the MB, via the process known as the abscission (Figure 1A). Abscission is a highly regulated event, and it is now well established that the MB plays a key role in regulating completion of cytokinesis by recruiting and activating abscission-mediating proteins, such as the Endosomal Sorting Complex Required for Transport (ESCRT-III) complex, as well as several regulators of the abscission checkpoint[1, 2]. While targeting and activation of abscission regulators at the MB is required for completion of cytokinesis, the mechanisms governing this process remain to be fully defined.

Previous studies have shown that several members of the ESCRT-III machinery are recruited to the MB just before initiation of the abscission[3-6]. Specifically, it was shown that TSG101 recruits Charged Multivesicular Body Proteins (CHMPs, components of the ESCRT-III complex)[7] to the MB during telophase. In addition to TSG101, ALIX (also known as PDCD6IP) also contributes to the direct recruitment of the ESCRT-III complex to the MB[1, 4, 8]. Upon recruitment to the MB, the ESCRT-III components oligomerize (CHMP4B and CHMP2A or CHMP3 and CHMP6) into spiral structures with progressively smaller diameters towards the abscission site[9-11], the process that is thought to be responsible for the eventual abscission of the intercellular bridge to complete cytokinesis and form two daughter cells[6, 9, 10]. Inhibiting MB recruitment of ESCRT-III results in abscission defects, demonstrating the importance of appropriately regulating ESCRT-III protein accumulation and activation at the MB[5, 6, 12-15].

Until recently, it has been thought that TSG101 accumulates at the MB by binding to the MB resident protein, CEP55[3, 4, 6, 9, 10, 16, 17]. This binding was presumed to tether the TSG101 at the MB, gradually leading to ESCRT-III accumulation before initiation of abscission. However, recent studies have shown that depletion of CEP55 does not fully block ESCRT-III targeting to the MB, and CEP55 knock-out mice are able to grow and develop[18]. Finally, CEP55 is a protein present only in vertebrates, thus, while CEP55 clearly contributes to ESCRT-III recruitment to the MB in vertebrates, it does not appear to be absolutely required for abscission. Additionally, the MB and intercellular bridge are microtubule-rich, diffusion-limited structures, raising a question of how large protein complexes, such as the ESCRT-III complex, can rapidly diffuse via the intercellular bridge into the MB from the cytosol in a timely and efficient manner.

Recent work suggested that in addition to regulating abscission, secreted post-mitotic MBs (also known as MBsomes, MB remnants, or Flemmingsomes) can be internalized by other cells where they regulate cell proliferation and differentiation[8, 19-24]. It was proposed that these MBsomes may mediate cell-to-cell transfer of various signaling molecules in a manner similar to exosomes and extracellular vesicles[23, 24]. Consequently, several laboratories, including ours, have analyzed the proteome of secreted MBsomes. Interestingly, these studies have shown that, in addition to various signaling proteins, MBs are also enriched in ribosomal and translation initiation factor proteins[8, 23-25], raising an intriguing possibility that MB-associated mRNA targeting and localized translation may mediate various mitotic and post-mitotic MB functions.

In this study we show, for the first time, that a specific subset of mRNAs is indeed targeted to and enriched at the MBs. We also demonstrate that MBs contain active ribosomes and that MB-associated protein translation is needed for successful completion of the abscission. Importantly, by using a combination of RNAseq, qPCR, and smFISH, we demonstrate that mRNA encoding ESCRT-III components, specifically CHMP4B, CHMP2A, CHMP3, and CHMP6, are all enriched at the MB, and that MB-associated translation is needed for CHMP4B accumulation at the MB during telophase. Additionally, characterization of CHMP4B mRNA revealed that the 3′ UTR is critical for efficient CHMP4B mRNA targeting to the MB. Finally, we identify GA-rich localization elements within 3′ UTR that are necessary and sufficient to target mRNA to the MB. Collectively, this study proposes a novel mechanism of regulating cytokinesis and abscission by MB-associated targeting and localized translation of selective mRNAs that include, but are not limited to, the members of ESCRT-III complex. These findings lay a foundation for future studies in determining the molecular mechanisms regulating mRNA targeting and translation at the MB, and future analyses of the roles that this mRNA targeting plays in regulating abscission and post-mitotic MBsome functions.

Results

Identification of Midbody-Associated mRNAs

103 Recent studies have shown that MBs are enriched in RNA-binding proteins[8, 23-25], leading to the
104 intriguing idea that MBs may contain mRNAs, and that local translation at the MB may regulate
105 various MB functions. To test this hypothesis, we first set out to determine whether specific
106 mRNAs actually accumulate at the MBs and began by isolating MBsomes from tissue culture
107 media as previously described[26] (Figure 1A). We then prepared oligo-dT-based mRNA libraries
108 from MBsomes and matched whole cell RNA samples, analyzing them using RNAseq
109 (Supplemental Table 1). To assess the reproducibility of the RNA content of our MBsome
110 preparations and their relationship to whole cell RNA samples, we used principal components
111 analysis and hierarchical clustering (Figure 1B, C). With both approaches, we found that the MB
112 RNA samples were highly similar to each other, indicating the reproducible nature of their RNA
113 contents. Importantly, they were well separated from the whole cell RNA samples, suggesting
114 that the MB RNA samples contained an mRNA composition distinct from that found in the whole
115 cell samples. Overall, the RNAseq analysis identified 16,922 mRNAs that can be detected in
116 the MBsome. From those, 505 mRNAs were significantly depleted and 705 mRNAs were
117 significantly enriched in the MBsomes as compared to the whole cell RNA samples (Figure 1D;
118 Supplemental table 1).
119
120 MBsomes are produced exclusively by mitotic cells. Our observed MBsome-enriched RNAs,
121 then, could therefore simply reflect the RNA content of cells that produced MBsomes (i.e. cells
122 undergoing mitosis) rather than RNAs specifically trafficked to the midbody. To assess whether
123 our observed MBsome RNA enrichments reflected MBsome-localized RNAs or the general RNA
124 content of mitotic cells, we compared our data to RNAseq data from unsynchronized HeLa cells
125 sorted for cell cycle phase using Fucci reporter expression[43]. For all RNAs, we calculated their
126 relative enrichment in cells in G2/M phase compared to cells in G1. We found that our MBsome-
127 enriched RNAs were significantly less abundant in G2/M cells compared to G1 cells (Figure
128 S1A). Similarly, MBsome-enriched RNAs were less abundant in cells in S phase compared to
129 G1 cells (Figure S1B). From these data, we conclude that RNA enrichments in MBsomes are
130 not due to their increased abundance in mitotic cells.
131
132 Given the MB's connection to the mitotic spindle, we also wondered whether MBsome-enriched
133 RNAs were generally localized to the mitotic spindle or were specific to the MB. To test this, we
134 analyzed RNAseq data in which spindle-associated RNAs were identified through differential
135 centrifugation[44]. We found that MBsome-enriched RNAs were not spindle-enriched, indicating
136 that these two RNA populations are likely distinct (Figure S1C).
137
138 To determine the possible function of these MB-enriched mRNAs, we performed a Gene
139 Ontology (GO) Enrichment Analysis (Figure 2A) and found that mRNAs encoding for proteins
140 that regulate cell cycle and microtubule dynamics are enriched at the MBsomes (Figure 2A). We
141 also determined that mRNAs of several abscission-regulators, such as Citron Kinase, CDK11A,
142 CDK11B, and AKTIP, are also enriched in the MBsomes (Figure 2B). Importantly, we found that
143 mRNAs of the ESCRT-III complex proteins, CHMP4B, 2A, 3, and 6, were all enriched at the
144 MBsome (Figure 2B-D). This is especially noteworthy as CHMP4B/2A and CHMP3/6 are known
145 to co-polymerize and drive the final abscission step[9-11] (Figure 2D), suggesting that localized
146 translation of ESCRT-III proteins may drive their accumulation at the MB and may also be
147 required for the abscission step of cytokinesis.
148
149 Interestingly, not all mRNAs of genes associated with abscission were found to be enriched at
150 the MBsomes. For example, CEP55, TSG101, ALIX, and VPS4 mRNAs, while present in
151 MBsomes, were not enriched as compared to the whole cell transcriptome (Figure 2B-C). This
152 suggests that only a subset of abscission regulating proteins, specifically proteins that act during
153 final steps of the abscission, may be controlled by local translation. Consistent with this

154 hypothesis, CEP55, TCG101, and ALIX regulate early steps of the abscission, namely recruiting
155 and tethering ESCRT-III to the MB (Figure 2D). In contrast, all ESCRT-III components are
156 recruited during late telophase, just before completion of the abscission, suggesting an
157 intriguing possibility that the MB targeting of proteins during telophase may depend on localized
158 translation of specific mRNAs after MB formation. In the rest of the study, we will test this
159 hypothesis by focusing on the machinery mediating MB targeting and translation of CHMP4B
160 mRNA.
161
162 ***Midbodies contain the molecular machinery required for protein translation***
163 Our GO analysis (Figure 2A) demonstrated that numerous MB-associated mRNAs encode for
164 proteins that regulate ribosomal assembly and function. This further supports the idea that MBs
165 contain ribosomal machinery, which in turn can mediate local translation. Due to this finding,
166 and the fact that CHMP4B mRNA is enriched in the MBs, we hypothesized that local translation
167 of CHMP4B and other ESCRT-III subunits may contribute to ESCRT-III accumulation at the MB,
168 therefore regulating the abscission. For this hypothesis to be correct, MBs must contain
169 CHMP4B mRNA and translation associated ribosomal machinery, as well as be sites of active
170 protein translation.
171
172 To test this idea, we first visualized CHMP4B mRNA using single molecule inexpensive RNA *in*
173 *situ* hybridization (smiFISH)[27]. Consistent with our hypothesis that CHMP4B may be translated
174 at the MB, we found that CHMP4B mRNA is present within the intracellular bridge during
175 telophase (see arrows in Figure 3A) in over 60% of dividing HeLa cells (Supplemental Figure
176 2C-D). To validate the specificity of our CHMP4B smFISH probes, we depleted CHMP4B RNA
177 using siRNA and observed a corresponding decrease in the number of observed CHMP4B RNA
178 molecules per cell (Figure 3B).
179
180 There are multiple mechanisms that can drive mRNA accumulation at specific subcellular
181 compartments. One is direct targeting of mRNA that is independent of translation, and
182 another is co-translational targeting of mRNA that relies on the targeting of the nascent peptides
183 (rather than mRNA) that emerge from the ribosome during translation. In this case, mRNA is
184 indirectly accumulated to the specific subcellular compartment as the result of protein-
185 dependent targeting of the entire mRNA-associated ribosome. To differentiate between these
186 two possibilities, we briefly treated the cells with puromycin, a known inhibitor of protein
187 translation that dissociates ribosomes from their mRNA substrates. As shown in Supplemental
188 Figure 2A,C-D, puromycin treatment did not block CHMP4B mRNA accumulation at the MB,
189 suggesting that localized protein translation is not required for the mRNA targeting to the MB.
190
191 Next, we set out to determine if ribosomal components that are needed for translation are also
192 present at the MB. Initially, we analyzed three different proteomic datasets of purified MBsomes
193 using The Database for Annotation, Visualization, and Integrated Discovery (DAVID)[8, 23, 24].
194 Consistent with the possibility of localized MB-associated translation, there are numerous
195 ribosomal and translation initiation factor proteins present in the MB proteome (Figure 3C). Not
196 only were there ribosomal and translation initiation factor proteins present in the proteomic
197 datasets, but they were also highly enriched according to the DAVID analysis enrichment score
198 (Figure 3C). Finally, upon staining HeLa cells with antibodies against Ribosomal Protein L3
199 (RPL3), we observed the presence of RPL3 in the MB and intracellular bridge (marked by anti-
200 Acetylated-Tubulin antibodies) (Figure 3D-F). While this does not prove that local translation is
201 occurring, it supports the idea that the ribosomal translation machinery is present at the MB and
202 can potentially perform active translation of MB-associated mRNAs.
203
204 ***Midbodies are sites for active translation***

While the presence of ribosomal machinery at the MB supports the idea of local MB-associated protein translation, it is yet to be shown that active translation actually occurs at the MB and intracellular bridge during late telophase. To test this possibility, we used puromycin as a marker for active translation. Puromycin inhibits translation by causing the formation of a puromycylated nascent peptide chain and leading to dissociation of ribosomes and premature chain release. Importantly, these puromycylated peptides accumulate at sites of active translation and can be detected using anti-puromycin antibodies. To test whether translation occurs at the MB, we treated HeLa cells for 10 min with either DMSO or puromycin. We found that an anti-puromycin signal in MBs can be observed in puromycin-treated cells (Figure 4A-D), and, importantly, pre-treatment of cells with cycloheximide (Figure 4A) blocked the anti-puromycin signal (Figure 4A-D). Cycloheximide functions by interfering with the translocation step in protein synthesis, thus preventing ribosomes from incorporating puromycin in nascent peptides. Finally, anti-CHMP4B and anti-puromycin signals co-localized at the MB and intercellular bridge (Figure 4E-H). The presence of anti-puromycin signal in the MB and intracellular bridge is consistent with our hypothesis that MB-enriched mRNAs are locally translated during telophase. However, it is important to note that our experiments do not rule out the possibility that puromycylated nascent peptides could be generated in the cell body and then diffuse into the MB. Considering that MBs are diffusion limited structures (due to high cross-linking of MB microtubules) and short treatment time (only 10 min) we consider that unlikely. However, further experiments will be needed to fully demonstrate that CHMP4B is translated at the MB (also see Figure 8).

Active translation is required for the accumulation of CHMP4B at the MB during late telophase

Since our data suggest that local translation may occur in the MB, and that the anti-puromycin signal co-localizes with CHMP4B, we hypothesized that inhibiting protein translation at the MB should affect CHMP4B accumulation at the MB during late telophase. To test this hypothesis, we briefly (1 hour) treated HeLa cells with puromycin to block translation and analyzed endogenous CHMP4B levels at the MB by immunofluorescence microscopy. Consistent with our hypothesis, puromycin-treatment decreased CHMP4B intensity in the MB (Figure 5A-C). CHMP4B levels were also slightly reduced in the cell body, although to a much lesser (and statistically not significant) extent than seen in the MB (Figure 5A, D, and E).

Puromycin blocks all protein translation. Consequently, even a short puromycin treatment will impact many proteins, thus, it is possible that inhibition of translation also affects other MB proteins. To further bolster this idea, we chose to look at CEP55, a protein that is recruited to the MB during its formation and is required for MB-accumulation of TSG101 and ESCRT-III complex (including CHMP4B) [3, 4, 6, 9, 10, 16, 17]. Since CEP55 mRNA was not found to be enriched in our RNAseq analysis (Figure 2B), it presumably does not require MB-associated translation for its targeting. Consistent with this hypothesis, puromycin treatment did not have any effect on CEP55 intensity in the MB or cell body (Figure 5F-J).

The experiments described above used non-synchronized cells. Consequently, we cannot discount the possibility that 1 hour puromycin treatment affected CHMP4B mRNA translation during metaphase and anaphase before the formation of the MB. If that was the case, the differences we observed in CHMP4B accumulation at the MB would be the result of translation inhibition in the cell body (before telophase) rather than MB. To discount this possibility we next synchronized HeLa cells stably expressing GFP-MKLP1 using a thymidine/nocodazole block (Supplemental Figure 3A). Cells in metaphase were then washed to release from the block and incubated in serum-supplemented media for 90 minutes at 37°C followed by fixation and staining with (Supplemental Figure 3A). We have previously shown that within this 90-minute

255 incubation cells progress from metaphase to telophase[45], and, consistent with our previous
256 work, we observed that over 90% of cells were in late telophase with clearly visible CHMP4B
257 present at the MB (Supplemental Figure 3B). Importantly, the addition of puromycin for the last
258 30 minutes of the 90-minute incubation significantly decreased accumulation of endogenous
259 CHMP4B at the MB (Supplemental Figure 3B-C).
260
261 If localized translation of CHMP4B, and presumably other members of the ESCRT-III complex,
262 is required for their accumulation at the MB, we would expect that inhibition of translation during
263 telophase would affect the cells' ability to undergo abscission, by arresting them at late
264 telophase. To test this hypothesis, we counted the number of cells in telophase and found that 1
265 hour of treatment with puromycin significantly increased the number of cells in telophase (Figure
266 5K), while decreasing the number of cells that have just undergone abscission (Figure 5L;
267 Supplemental Figure 4A-D), which are all indications of defects in cell division.
268
269 To further test whether puromycin can delay cell abscission we next imaged telophase cells
270 expressing GFP-MKLP1 for 90 minutes by time-lapse microscopy (Supplemental Figure 4E-F).
271 In all cases we selected cells that were already in telophase, as indicated by the flattened cell,
272 round nucleus, and presence of a GFP-MKLP1 labeled MB. Consistent with several previous
273 studies, all cells (5 out of 5 imaged) in telophase successfully divided within 75 minutes
274 (Supplemental Figure 4E; asterisk marks the MB; arrow points to abscission site). In contrast,
275 none of the telophase cells (0 out of 5 imaged) completed abscission within 90 minutes if
276 puromycin was added at the beginning of time-lapse analysis.
277
278 While the previous experiments support the idea that local translation of CHMP4B is at least
279 partially responsible for the accumulation of CHMP4B during telophase, it does not exclude
280 other mechanisms for CHMP4B accumulation at the MB. Since it has been proposed that
281 CEP55 is the key initial recruiter of abscission-related proteins in mammalian cells, it is plausible
282 that both pathways are required for efficient recruitment of ESCRT-III during abscission. To
283 further test this idea, we used puromycin, CEP55 siRNA, or CEP55 siRNA/puromycin
284 treatments and tested their effect on CHMP4B accumulation in the MB. As we already have
285 shown, puromycin treatment alone caused a significant reduction in CHMP4B intensity at the
286 MB (Figure 5M-O). Similarly, consistent with previous reports, CEP55 knock-down
287 (Supplemental Figure 2B) also decreased CHMP4B intensity at the MB (Figure 5M-O). This
288 decrease was not due to a decrease in *CHMP4B* mRNA accumulation at the MB (Supplemental
289 Figure 2E) but likely due to lack of CEP55-dependent tethering of Alix and TSG101 at the MB
290 (Figure 2D). Surprisingly, a combination of CEP55 KD and puromycin treatment did not further
291 reduce CHMP4B intensity at the MB, suggesting that local MB-associated translation and
292 CEP55 may work together to allow efficient accumulation (by localized translation) and retention
293 (by tethering CHMP4B at the MB) of CHMP4B during late telophase.
294
295 ***Short puromycin wash-out recovers CHMP4B levels at the MB but not cell body***
296 While our previous data shows that MB-localized protein translation contributes to CHMP4B
297 accumulation at the MB, the data are somewhat difficult to interpret because puromycin also
298 resulted in a slight decrease of CHMP4B levels in the cell body. Thus, we could not fully
299 differentiate between two possibilities: (1) CHMP4B targeting relies on MB-associated
300 translation during telophase; (2) CHMP4B is translated at the cell body and then simply diffuses
301 back to the MB. To help differentiate between those two possibilities we performed a puromycin
302 wash-out experiment (Figure 6). Briefly, we treated cells with puromycin for 1 hour, followed by
303 a quick puromycin wash-out and incubation of cells for 5 or 10 minutes, before analyzing the
304 levels of CHMP4B in the MB and the cell body. As we already have shown, puromycin
305 treatment resulted in decreased CHMP4B levels in both the MB and the cell body (Figure 6A-E).

306 Importantly, after puromycin wash-out, CHMP4B levels at the MB started to increase within 5
307 min, with a complete recovery after 10min (Figure 6A, B-C). On the contrary, CHMP4B intensity
308 in the cell body did not recover even after 10min (Figure 6A, D-E), suggesting that CHMP4B
309 accumulation at the MB is primarily driven by localized translation rather than by diffusion of
310 CHMP4B from the cell body.
311
312 Since CHMP4B levels rapidly recover at the MB after the puromycin wash-out, this should also
313 lead to a rapid recovery of the cell's ability to undergo abscission. Consistent with this idea, 5
314 minutes after the puromycin wash-out, cells fully recovered their ability to undergo abscission,
315 as determined by a decrease in number of cells in telophase and increase in number of cells
316 that have just undergone abscission (Figure 6F). All this data suggests that CHMP4B
317 accumulation at the MB depends on local translation rather than diffusion from the cell body,
318 and that MB-associated translation of CHMP4B is required for successful completion of the
319 abscission.
320
321 ***The 3′ UTR of CHMP4B mRNA enhances CHMP4B protein accumulation at the MB***
322 Up to this point, we have been able to show that CHMP4B mRNA is present in the MB, local
323 translation may occur at the MB, and that CHMP4B accumulation at the MB is at least partially
324 regulated by local translation. The next step was to determine how the *CHMP4B* mRNA is
325 targeted to the MB. RNA trafficking is often driven by cis-regulatory localization elements (LEs)
326 that are commonly found in the 5'- or 3′ UTRs[28]. To that end, we generated clones containing
327 the 5'- and/or 3′ UTR of *CHMP4B* fused to RFP-*CHMP4B* cDNA. One major issue with transient
328 expression is the high variation in expression levels in different cells hindering our ability to tell
329 whether differences in MB targeting of various *CHMP4B* constructs are due to UTRs or due to
330 the differences in expression levels. To minimize this issue, we used a HeLa LoxP
331 recombination system[29]. Briefly, this system uses *cre* recombination to allow for single copy,
332 site-specific recombination of our constructs into the HeLa genome[29]. This allowed us to obtain
333 virtually homogenous cell pools containing various doxycycline-inducible *CHMP4B* constructs.
334 Importantly, each cell in these pools will have one copy of the construct that is inserted at the
335 same genomic locus. Upon making cell lines containing various *CHMP4B* constructs, we first
336 used immunofluorescence microscopy, western blotting, and qPCR to confirm that doxycycline
337 does induce the expression of these constructs to the approximately the same level
338 (Supplemental Figure 4A-G). Interestingly, we found that the presence of *CHMP4B* 3′ UTR
339 without the 5′ UTR slightly deceased *CHMP4B* mRNA levels, raising the possibility that the 3′
340 UTR of CHMP4B may also regulate mRNA stability (Supplemental Figure 4B and E).
341 Additionally, please note that the insertion of the 5′ UTR generated an alternative start codon
342 that was in frame with the RFP, resulting in two CHMP4B bands on Western blots
343 (Supplemental Figure 4F).
344
345 To determine the role of UTRs in CHMP4B targeting, we first tested whether having the 5'-
346 and/or 3′ UTR of *CHMP4B* resulted in more efficient RFP-CHMP4B accumulation in the MB. To
347 that end, we calculated the ratio of RFP-CHMP4B protein intensity at the MB and cell body. As
348 shown in the figure 7A-C, the presence of the 3′ UTR significantly enhanced RFP-CHMP4B
349 enrichment at the MB as compared to RFP-CHMP4B alone (Figure 7A-C). Interestingly, the 5′
350 UTR alone did not enhance RFP-CHMP4B targeting to the MB, nor did it enhance the effect of
351 3′ UTR (Figure 7A-C). All this data suggests that the 3′ UTR plays an important role in mediating
352 CHMP4B protein accumulation in the MB during telophase, presumably due to targeting and
353 localized translation of RFP-CHMP4B mRNA. Consistent with previous reports, RFP-CHMP4B
354 without UTRs is still able to accumulate in the MB, although at much lower levels as compared
355 to RFP-CHMP4B-3′UTR, potentially showing that there are multiple mechanisms, such as
356 CEP55 binding, that drives ESCRT-III targeting during abscission.

It has been previously reported that over-expression of exogenous tagged ESCRT-III members inhibits abscission[13]. Consistent with those studies, we also see an increase in multinucleation and the number of telophase-arrested cells in the cells overexpressing RFP-CHMP4B (Figure 7D-E). While the cause of this inhibition remains to be fully understood, it has been suggested that CHMP4B overexpression may lead to accumulation of cytosolic ESCRT-III aggregates, thus, sequestering the rest of the ESCRT-III subunits away from the MB. We wondered whether the inhibitory effect of exogenous CHMP4B may be due to the fact that it's mRNA lacks localization elements mediating targeting of CHMP4B to the MB. Consistent with this hypothesis, the effect of over-expression on multinucleation or telophase arrest was reversed in cell lines expressing RFP-CHMP4B constructs containing 3′ UTR (Figure 7D-E).

The 3' UTR of CHMP4B mRNA is required for its targeting to the MB

Since the 3′ UTR of *CHMP4B* RNA is important for CHMP4B protein accumulation at the MB during abscission, it might be expected that the 3′ UTR is also important for *CHMP4B* mRNA targeting to the MB. To determine that, we first analyzed *RFP-CHMP4B* mRNA localization using smiFISH probes against *CHMP4B*. Consistent with the requirement of the 3′ UTR for RFP-CHMP4B accumulation, we observed smiFISH signal in the MB of cells only expressing the RFP-CHMP4B-3′UTR construct (Figure 7F). One drawback of using smiFISH in the MB is that it is only semi-quantifiable due to not knowing how efficiently the probes are able to penetrate the protein-rich region. To better quantify the difference between *RFP-CHMP4B* mRNA targeting to the MB, we purified MBsomes from cell lines expressing various constructs and analyzed mRNA levels by performing RT-qPCR on purified MBsomes and then compared them to whole cell mRNA levels. To measure only exogenous *CHMP4B* RNA, we used primers designed to target the *RFP* sequence. As shown in Figure 7G, the presence of the 3′ UTR was required for efficient *RFP-CHMP4B* mRNA targeting to the MB, as compared to the amount of *RFP* mRNA alone or *RFP-CHMP4B* mRNA without 3′ UTRs (Figure 7G). This data suggests that the 3′ UTR is required for efficient *RFP-CHMP4B* mRNA targeting to the MB. Interestingly, *RFP-CHMP4B* RNA without UTRs was also slightly enriched at the MB as compared to *RFP* RNA alone. This slight mRNA enrichment could be due to co-translational *RFP-CHMP4B* mRNA accumulation at the MB. To test this possibility, we removed the start codon and generated a HeLa cell line expressing doxycycline-inducible RFP-CHMP4B-NoStart construct (Supplemental Figure 4C and E) and tested whether this mRNA also accumulates at the MBs. As shown in Figure 7E, removal of the start codon did not affect the ability of *RFP-CHMP4B* mRNA to accumulate at the MB, although it was clearly still much lower than *RFP-CHMP4B-3'UTR*. All this data suggests that the 3′ UTR is required for efficient CHMP4B mRNA targeting, although the coding sequence also appears to contribute to mRNA accumulation at the MB.

To test whether the 3′ UTR of CHMP4B is sufficient for the targeting of any mRNA to the MB, we generated a doxycycline inducible RFP-only construct that contained the 3′ UTR from *CHMP4B* (RFP-3'UTR; Supplemental Figure 4D and E) and tested the mRNA levels at the MB. As shown in the figure 7E, 3′ UTR of *CHMP4B* did slightly enhance the levels of *RFP* mRNA at the MB, although it did not reach the levels of *RFP-CHMP4B-3'UTR* mRNA. This suggests that while *CHMP4B* 3′ UTR is essential for mRNA targeting, it may require other targeting elements that are possibly present in the *CHMP4B* coding region or secondary structure of the coding region to get the full targeting of mRNA to the MB.

The 3' UTR of CHMP4B mRNA is required for its localized translation at the MB

Since the 3′ UTR is required for *CHMP4B* mRNA targeting to the MB, we wondered whether it may also be required for localized CHMP4B translation at the MB. If CHMP4B is locally translated at the MB, it would be expected to start accumulating at the MB during late telophase

408 after the formation of the MB. Indeed, it has been previously shown that endogenous CHMP4B
409 accumulates at the MB just before the abscission, while CEP55, TSG101, and Alix are known to
410 be present at the MB from the very beginning of MB formation. To understand the timing and
411 dynamics of RFP-CHMP4B accumulation at the MB we next performed a time-lapse analysis of
412 cells stably expressing *RFP-CHMP4B-3'UTR* mRNA (Figure 8A). To minimize the possibility
413 that RFP-CHMP4B diffuses from the cell body we chose cells in late telophase (as determined
414 by round nuclei and flattened body) that were still connected with a long intracellular bridge
415 (Figure 8A, MB marked by asterisk). As shown in the figure 8A, RFP-CHMP4B was initially
416 absent in the MB (see time point 0 min), but then started accumulating with the MB over 10-30
417 minutes, the dynamics consistent with translation of CHMP4B at the MB during late telophase.
418
419 While the time-lapse analysis of cells expressing *RFP-CHMP4B-3'UTR* mRNA is consistent with
420 the possibility that RFP-CHMP4B is locally translated at the MB, it does not directly demonstrate
421 that CHMP4B is locally translated and that the 3′ UTR is required for this process. To more
422 directly investigate that, we overexpressed an N-terminally HA-tagged CHMP4B construct with
423 or without *CHMP4B*'s 3′ UTR. Cells were then treated for 10 minutes with puromycin, followed
424 by fixation and incubation with anti-HA and anti-puromycin antibodies. We next analyzed fixed
425 cells with proximity ligation assay (PLA). The idea of this experiment is that the accumulation of
426 nascent peptides containing HA (at the N-terminus) and puromycin (more towards the C-
427 terminus) will be an indication of local translation and can be detected by HA/puro PLA.
428 Importantly, since the 3′ UTR of *CHMP4B* is required for *HA-CHMP4B* mRNA targeting to the
429 MB, we should not detect PLA signal in cells overexpressing HA-CHMP4B lacking the 3′ UTR.
430 This experiment also allowed us to test whether diffusion from the cell body of puromycylated
431 nascent peptides is sufficient to generate PLA signal in the MB (also see experiments shown in
432 Figure 4). As shown in the figure 8B-D, we could indeed detect HA/puro PLA signal in the cells
433 expressing *HA-CHMP4B-3'UTR*. This signal was significantly diminished in cells expressing HA-
434 CHMP4B without 3'UTR. Importantly, the PLA signal was essentially absent in cells not treated
435 with puromycin or cells not expressing the HA-tagged CHMP4B construct (Figure 8C-D). Taken
436 together, all these data demonstrate that 3′ UTR is required for *CHMP4B* mRNA targeting to the
437 MB and is also needed for localized CHMP4B translation at the MB during late telophase.
438
439 ***The MBsome transcriptome is similar to other localized transcriptomes associated with***
440 ***the plus-ends of microtubules***
441 We next sought to identify specific *cis*-elements (LEs) within MBsome-enriched RNAs that
442 regulated their trafficking to the MB. We recently identified RNA elements that were necessary
443 and sufficient for transport to both the neurites of neuronal cells and the basal pole of epithelial
444 cells[40]. Both of these subcellular locations are associated with the plus ends of microtubules,
445 and we showed that these RNA elements directed RNAs to their destinations by targeting them
446 to microtubule plus ends. Given that MBs are associated with the plus-ends of microtubules
447 emanating from each daughter cell, we reasoned that perhaps the same regulatory elements
448 and mechanisms that drive RNAs to neurites and the basal pole of epithelial cells would also
449 drive mRNAs to MBs.
450
451 If this were true, we would expect the same sets of mRNAs to be enriched at all three
452 subcellular locations. To test this, we asked whether our MBsome-enriched RNAs were more
453 neurite-enriched than other RNAs. For this comparison, we used a previously published dataset
454 in which mouse neuronal cells were mechanically fractionated into soma and neurite fractions
455 followed by analysis of their RNA contents using RNAseq[46]. We compared the neurite-
456 enrichments of the mouse orthologs of our MBsome-enriched RNAs to the neurite-enrichments
457 of all other mouse RNAs. We found that the mouse orthologs of the MBsome-enriched RNAs

458 were significantly more neurite-enriched than all other RNAs, suggesting that neurites and
459 MBsomes contain similar mRNA contents (Figure 9A).
460
461 Using data from human intestinal epithelial cells[40], we then compared enrichments across the
462 apicobasal axis for MBsome RNAs and all other detected RNAs. Again, we found that MBsome-
463 enriched RNAs were significantly enriched at the basal pole of these cells compared to non-
464 MBsome-enriched RNAs (Figure 9B). Taken together with the neurite RNA enrichments
465 observed above, this indicates that neurites, the basal pole of epithelial cells, and MBsomes are
466 enriched for similar sets of mRNAs, implying that similar mechanisms (e.g. plus-end directed
467 transport along microtubules) may be populating their transcriptomes.
468
469 ***Identification of 3' UTR localization elements that are necessary and sufficient to target***
470 ***mRNA to the MB***
471 Our previous studies that identified mechanisms behind RNA transport along microtubules
472 focused on the *Net1* mRNA[40,47]. These studies identified a GA-rich 260 nt region within the 3′
473 UTR of *NET1* that was both necessary and sufficient to direct RNA to the plus ends of
474 microtubules in both neuronal and epithelial cells. We therefore wondered if the same element
475 had similar abilities to direct RNA transport to the MB and MBsomes.
476
477 We started by asking if endogenous *NET1* mRNA was enriched in our MBsome RNA samples
478 (Figure 1D) since our previous studies had found *NET1* mRNA enriched in the neurites[47], and
479 we observed *NET1* mRNA enriched at the basal pole of intestinal epithelial cells (Supplemental
480 Figure 6A, B). We found that *NET1* mRNA was approximately 4-fold enriched in MBsomes
481 relative to whole cells (Figure 9C). This observation was confirmed with smiFISH, showing
482 *NET1* mRNA puncta in close proximity to MBs in dividing cells (Figure 9D). After quantifying the
483 smiFISH results across many cells, we found that *NET1* mRNA was more likely to be enriched
484 at both the intracellular bridge (Figure 9E) and the midbody (Figure 9F) compared to the control
485 transcript *TSG101* (that is not enriched in MBs as measured by RNAseq and qPCR; see Figure
486 2).
487
488 We next asked if the same RNA *cis*-regulatory element within mouse *Net1* mRNA previously
489 shown to promote RNA trafficking to neurites and the basal pole of epithelial cells also
490 controlled RNA localization to MBs and MBsomes. To test this, we devised an RT-qPCR-based
491 reporter assay that quantified the enrichment of designed reporter transcripts in MBsomes
492 (Figure 10A). In this assay, Firefly and Renilla luciferases are co-expressed from a bidirectional
493 promoter with the Renilla luciferase RNA serving as an unchanging internal control. RNA from
494 MBsomes and whole cells was collected as described before, and the relative amounts of Firefly
495 and Renilla luciferase transcripts in each fraction was determined using Taqman RT-qPCR. By
496 comparing how the ratios of these transcripts vary between cell fractions depending on the 3′
497 UTR appended to the Firefly luciferase RNA, we are able to quantify the ability of the 3′ UTR to
498 drive the Firefly luciferase transcript to MBsomes.
499
500 We created four Firefly luciferase reporter RNAs (Figure 10B). These reporters contained 3′
501 UTRs consisting of the entire *Net1* 3′ UTR, the previously identified 260 nt element within the
502 *Net1* UTR that was sufficient to drive RNA transport to neurites and the basal pole of epithelial
503 cells, the entire *Net1* UTR lacking this element, and as a control, an unrelated plasmid-encoded
504 UTR. These constructs were site-specifically incorporated into HeLa cells using *cre*/loxP
505 recombination, and their expression was controlled using a doxycycline-on system.
506
507 We then measured the relative MBsome-enrichment of each of these constructs using the RT-
508 qPCR strategy outlined in Figure 9A, setting the enrichment of the reporter with the control 3′

UTR to one. We found that the addition of the entire *Net1* UTR to the reporter construct increased its MBsome-enrichment by approximately 2-fold (Figure 10C). The reporter containing the previously identified 260 nt subset of the *Net1* UTR was similarly enriched in MBsomes, indicating that this *cis*-element is sufficient to drive RNAs to MBsomes. Deletion of this element completely abrogated the ability of the *Net1* 3′ UTR to regulate MBsome RNA localization, demonstrating that the element is also necessary for RNA transport to MBsomes.

Next, we confirmed these results using an orthogonal smFISH assay that visualized Firefly luciferase reporter RNAs *in situ*. The fluorescent probes used in this assay targeted the Firefly luciferase coding sequence that was shared across all reporter RNAs. As with the RT-qPCR approach, we found that the 260 nt *cis*-element within the *Net1* UTR was both necessary and sufficient for reporter RNA targeting to both MBs and the intercellular bridge of dividing cells (Figure 10D, E, Supplementary Figure 6C).

These results demonstrate that discrete RNA *cis*-regulatory elements control the RNA content of MBs and MBsomes and suggest that previously defined mechanisms that regulate microtubule-based RNA transport in other systems likely also act to populate the MBsome transcriptome[40].

Discussion

The midbody (MB) is a microtubule-rich structure that forms at the end of cytokinesis as the result of compacting central spindle microtubules during cleavage furrow ingression. Even though the MB was first identified over a hundred years ago, only in the last decade has it become apparent that the MB is not simply a byproduct of cell division but plays many important roles. It is now well-established that the MB functions as a scaffolding platform that recruits and activates many abscission regulating proteins, such as Aurora B kinase, MKLP1, and the ESCRT-III complex[16, 30-33]. Furthermore, recent studies have also shown that during cell division MBs can be released in the extracellular milieu where they are called MBsomes or Flemmingsomes[8, 23]. Uptake of these MBsomes by other cells can lead to changes in cell fate, differentiation, and proliferation capacity, presumably by mediating lateral transfer of specific signaling molecules[23, 24, 34]. However, what remains unclear is what these signaling molecules are and how they may affect cells after MBsome internalization. In this study we demonstrate that MBsomes contain a specific subset of mRNAs, many of them encoding proteins regulating cell division and differentiation. That raises a very intriguing possibility that delivery of specific mRNAs to the acceptor cells is what mediates post-mitotic MBsome functions, although further research will be needed to fully define the role of MBsome-dependent mRNA delivery.

Our study shows that MBs contain mRNAs encoding for several ESCRT-III components, namely CHMP2A, CHMP3, CHMP4B, and CHMP6. What makes this discovery especially exciting is that all these ESCRT-III complex proteins are known to co-oligomerize and drive the abscission step of cytokinesis. While the role of the ESCRT-III proteins in mediating abscission was first described over a decade ago[6, 9, 15], how ESCRT-III subunits are delivered and targeted to the MB remains somewhat controversial. Until recently, it has been thought that TSG101 and the ESCRT-III complex accumulate at the MB by directly or indirectly binding to MB resident protein, CEP55[3, 4, 6, 9, 10, 16, 17]. However, recent studies have shown that depletion of CEP55 does not fully block ESCRT-III targeting to the MB, and CEP55 knock-out mice are able to grow and develop with limited defects[18]. Additionally, CEP55 is only present in vertebrates, raising a question of how the ESCRT-III may be targeted in other organisms, although CEP55 clearly contributes to ESCRT-III targeting in vertebrate cells. Finally, the MB and intercellular bridge are packed with dense and heavily crosslinked microtubule bundles[35, 36], thus, creating a diffusion-limited environment. This raises the question about how large protein complexes, such as the

560 ESCRT-III complexes, can rapidly diffuse via the intercellular bridge into the MB from the
561 cytosol in a timely, efficient, and highly regulated manner. The discovery that ESCRT-III mRNAs
562 are enriched at the MB suggests an intriguing possibility that regulated localized translation of
563 ESCRT-III components contribute to accumulation of ESCRT-III at the MB during abscission.
564 This hypothesis is supported by results in other systems in which precise RNA localization is
565 critical for the successful association of the resulting translated protein with its proper interaction
566 partners[48].
567
568 Consistent with the hypothesis that localized protein translation contributes to ESCRT-III
569 targeting to the MB, we show that the MB has all the components needed for translation. We
570 also use anti-puromycin antibodies to demonstrate that active translation is occurring in the MB.
571 Finally, we show that inhibition of protein translation during late telophase blocks completion of
572 cytokinesis. Based on all these findings, we chose to further investigate one of the most
573 important regulators of late-stage abscission, CHMP4B. There are several pieces of evidence
574 suggesting that CHMP4B is being actively translated in the MB during telophase. First,
575 puromycylated CHMP4B nascent peptides are present at the MB. Second, inhibition of protein
576 translation during telophase leads to decrease in CHMP4B accumulation at the MB. Third,
577 wash-out of the translation inhibitor puromycin results in a very fast recovery of CHMP4B levels
578 at the MB, which could not be explained by simple diffusion of CHMP4B protein that was
579 translated in the cell body. Importantly, the ability of the cell to complete abscission also
580 recovers within a similar timescale. All of these data suggests that CHMP4B can be locally
581 translated and that it is at least partially responsible for the accumulation and function of
582 CHMP4B at the MB. Importantly, the mechanisms using of CEP55 and local translation to target
583 ESCRT-III to the MB are not necessarily mutually exclusive. Indeed, both of these mechanisms
584 appear to contribute to ESCRT-III localization in vertebrate cells suggesting that while localized
585 translation may be required to accumulate ESCRT-III components within the MB, CEP55 is
586 likely needed to tether and maintain their MB-enrichment during telophase.
587
588 Local translation of CHMP4B at the MB depends on the targeting of *CHMP4B* mRNA to the MB
589 during telophase. What remains unclear is the molecular machinery governing mRNA delivery
590 and accumulation at the MB. It has been previously shown that the subcellular targeting of
591 mRNAs is usually driven by *cis*-regulatory elements that are commonly found in the 5' or 3′
592 UTRs[28]. Consequently, we tested whether the 5' and 3′ UTRs are driving the translocation of
593 *CHMP4B* mRNA to the MB. Our data demonstrates that the 3′ UTR is required for translocation
594 and accumulation of CHMP4B at the MB. To test whether the 3′ UTR is sufficient for mRNA
595 accumulation at the MB, we added CHMP4B 3′ UTR to RFP and analyzed its ability to drive
596 RFP mRNA accumulation at the MB. Interestingly, while we did see an increase in the levels of
597 MB-associated *RFP* mRNA, the amount of *RFP-3'UTR* mRNA did not fully recapitulate the
598 levels of *RFP-CHMP4B-3'UTR* mRNA, suggesting that the *CHMP4B* coding region may also
599 play a role in *CHMP4B* mRNA targeting to the MB.
600
601 It has been previously shown that GA-rich motifs mediate targeting of *RAB13* mRNA targeting to
602 the actin rich cellular protrusions[37, 38]. Similarly, we have shown that GA-rich localization
603 elements (LEs) in mouse *Net1* mRNA can mediate *Net1* mRNA targeting to neurites and the
604 basal pole of epithelial cells[39]. Our RNAseq analysis of purified MBs showed that there is a
605 significant overlap between mRNAs targeted to the MB, neurite, and basolateral domains of
606 epithelial cells. Furthermore, *RAB13* and *NET1* mRNAs are also both enriched in the MB,
607 suggesting that their 3′ UTR GA-rich motifs may also mediate mRNA targeting to the MBs.
608 Consistent with this hypothesis, we show that the LE present in the 3′ UTR of mouse *Net1*
609 mRNA is necessary and sufficient to target mRNA to the MB. We recently found that these GA-
610 rich motifs likely target RNAs to neurites and the basal pole of epithelial cells by promoting their

transport to the plus ends of microtubules in a kinesin 1-dependent manner[40]. This type of transport would be perfect for targeting mRNAs to the MB as plus-ends of microtubules are oriented toward the MB, and kinesin 1 has already been implicated in transporting endosomes to the MB during cell division[41]. All these findings hint at a common mechanism that regulates the subcellular targeting of mRNAs across a variety of cell types and subcellular destinations.

Taken together, this is the first study to demonstrate that a specific subset of mRNAs are targeted and enriched at the MB during cell division and play a role in MB function during abscission (Figure 8). At least some of these mRNAs, such as *CHMP4B* mRNA, appear to be translated at the MB, and this translation plays a key role in accumulation of ESCRT-III components at the MB, thus regulating the abscission step of cytokinesis. While working out the details governing mRNA targeting and translation at the MB will require future studies, this work lays a foundation for the identification of a novel mechanism regulating abscission. Finally, this study will not only advance our understanding of the machinery governing ESCRT-III translocation and accumulation at the MB, but it could also provide novel insight into the mechanisms of RNA targeting to other subcellular compartments and other cell types, as well as providing a framework for studying the role of mRNAs in the post-mitotic MB function.

Materials and Methods

Cell culture

All HeLa cell lines were kept in a 37 °C humidified incubator at 5% CO2, routinely tested for mycoplasma, and were maintained in DMEM with 10% FBS and 1% penicillin/streptomycin.

Cell synchronization

HeLa cells were grown to ~50% confluency and incubated with 5 mM Thymidine for 16 hours. Cells were then washed and incubated with regular serum-containing media, filled by incubation with 0.1 ug/ml of nocodazole for 16 hours. Mitotic cells were then isolated by gently tapping tissue culture plates to dislodge loosely attached cells arrested in prometaphase. Cells were then washed, seeded on collagen-coated coverslips and incubated in serum containing media for 90 minutes in the presence or absence of puromycin (for last 30 minutes).

Reagents and antibodies

iTaq Universal SYBR Green Supermix was purchased from Bio-Rad. TRIzol, Puromycin, Doxycycline, Lipofectamine 2000, and Lipofectamine RNAiMax was purchased from Thermo Fisher Scientific. Stellaris Hybridization, Wash A, and Wash B Buffers were purchased from Biosearch Technologies. Hoechst stain was purchased from AnaSpec. Antibodies against the following proteins were used: RPL3 (Bethyl Laboratories #A305-007A,1:100 for immunofluorescence), Acetylated-Tubulin (Cell Signaling #D20G3, 1:500 for immunofluorescence), Acetylated-Tubulin (Millipore Sigma #T7451, 1:500 for immunofluorescence), CHMP4B (Proteintech #16639-I-AP, 1:300 for immunofluorescence), CEP55 (Abnova #H00055165-A01, 1:500 for immunofluorescence), RFP (Chromotek #6g6-20, 1:2000 for immunoblotting), Beta-Actin (LI-COR #926-42210, 1:2000 for immunoblotting), donkey anti-mouse-IgG conjugated to Alexa Fluor 488 (Jackson #715-545-150, 1:100 dilution for immunofluorescence), donkey anti-mouse-IgG conjugated to Alexa Fluor 594 (Jackson #715-585-1500, 1:100 dilution for immunofluorescence), donkey anti-rabbit-IgG Alexa Fluor 488 (Jackson #711-585-152, 1:100 dilution for immunofluorescence), and donkey anti-rabbit-IgG conjugated to Alexa Fluor 594 (Jackson #711-585-152, 1:100 dilution for immunofluorescence), donkey anti-mouse IRDye 680CW (LI-COR #926-32212, 1:5000 for immunoblotting), and donkey anti-rabbit IRDye 800CW (LI-COR #926-68072, 1:5000 for immunoblotting).

RNA isolation

RNA was extracted using Trizol (Thermo Fisher #15596026) per the manufacturer's instructions. The RNA was reverse transcribed using SuperScript IV (Thermo Fisher, #18091050) per the manufacturer's instructions.

RT-qPCR

Quantitative PCR was performed using iTaq Universal SYBR Green Supermix (Bio-Rad, #1725121). Primer sequences can be found in Supplemental Table 2. To quantify the RT-qPCR, each cDNA sample was normalized to GAPDH. If the experiment was looking at enrichment in MBsomes, the data is represented as a ratio of the normalized MB/normalized total cell. Taqman qPCR reactions were performed using Taqman Fast Advanced Master Mix (Life Technologies) with labeled probe sets (Supplemental Table 3). The quality of each Midbody isolation was quantified by the enrichment of NET1 in MBsomes using the ratio of NET1 / TSG101 in MBsomes compared to NET1/TSG101 in whole cells. Reporter enrichment in MBsomes was quantified using Renilla luciferase as internal control using the ratio of Firefly luciferase / Renilla luciferase RNA in MBsomes compared to the ratio of Firefly luciferase / Renilla luciferase RNA in whole cells.

MB purification and RNAseq

Midbodies were isolated as previously described[26]. Briefly, media from the various HeLa cells was collected and subjected to a series of centrifugation spins (300 × g, 10,000 × g). Sucrose gradient fractionation was performed at 3000×g, and the interphase between 40% glycerol and 2 M sucrose was collected, spun at 10,000 × g to pellet the midbodies. RNA was extracted using TRIzol (Thermo Fisher #15596026) per the manufacturer's instructions. For control and MB group 1, the library prep and RNAseq was performed by the University of Colorado Anschutz Medical Campus Genomics facility. The Genomics facility generated a poly A enriched library from the total RNA extraction and performed RNAseq on an Illumina HiSeq2000 platform, utilizing 1 lane, single read 125 cycles. For control group and MB group 2 and 3, the library prep and RNAseq was performed by Novogene. Briefly, Novogene generated a poly A enriched library from the total RNA extraction and performed RNAseq on a NovaSeq PE150 platform with 6 G raw data per sample.

RNAseq data processing

Transcript abundances were calculated using Salmon v1.9.0[42] using the flags –seqBias and –gcBias. Transcript abundances were collapsed to gene level using txImport [cite: https://f1000research.com/articles/4-1521/v1]. To determine enrichment of genes in the midbody, DEseq2 was used to calculate the log2 ratio of midbody/whole cell counts and identify significantly enriched RNAs[49]. Genes with a basemean (average of normalized count values) less than 250 were excluded. Plots were generated in Rstudio using R version 4.1.1.

siRNA transfections

Custom CHMP4B siRNA oligonucleotides (Dharmacon, AUCGAUAAAGUUGAUGAGUUAUU) and custom CEP55 siRNA oligonucleotides (Millipore Sigma, AGGCAUGUACUUUAGACUU) were transfected into HeLa cells using Liptofectamine RNAiMAX with 40nM oligonucleotide. The efficiency of the knock-down was measured 72 h post transfection by RT-qPCR (previously described above).

Immunofluorescence and quantification

HeLa cells were treated as indicated in the text and then fixed in 1% paraformaldehyde in PBS for 10 min at room temperature. Cells were rinsed three times in PBS. The cells were then incubated with primary antibody in PBS containing 0.5% BSA and 0.2% saponin for 1 h at room

712 temperature, washed three times in PBS and then incubated with the appropriate fluorochrome-
713 conjugated secondary antibodies diluted in PBS containing 0.5% BSA and 0.2% saponin for 30
714 min. Cells were washed three times in PBS and mounted in Fluoromount (Southern Biotech).
715
716 Fixed cells were imaged with an inverted Axiovert 200M microscope (Zeiss) with a × 63 oil
717 immersion lens and QE charge-coupled device camera (Sensicam). Z-stack images were taken
718 at a step size of 500–1000 nm. Image processing and quantification was performed using 3i
719 Slidebook 6 software (Intelligent Imaging Innovations). Briefly, masks were made to calculate
720 the total intensity of the cell body or the intercellular bridge as well as the total area for each
721 mask. The numbers were then used to calculate the intensity/micron^2. Unless otherwise stated,
722 all images are represented as a maximal projection of the z-stack.
723
724 *Time-lapse imaging*
725 HeLa cells stably expressing GFP-MKLP1 were plated on 6cm glass-bottom dishes and imaged
726 at 37^{0}C for 120 minutes with time lapse of 15 minutes (to minimize phototoxicity). To ensure that
727 cells are in mid-late telophase cells were selected based on following criteria: cells were
728 flattened with round nucleus (kidney-shaped nucleus is a feature of cells in early telophase)
729 containing identifiable MB (labeled by GFP-MKLP1). Where indicated, 25μM puromycin was
730 added at the beginning of time-lapse analysis.
731
732 *Proximal Ligation Assay*
733 HeLa cells stably expressing GFP-MKLP1 were transfected with either HA-CHMP4B or HA-
734 CHMP4B-3′UTR constructs. Non-transfected HeLa cells were used as one of the negative
735 controls. Cells were then treated with puromycin for 10 minutes (not treated cells were used as
736 another negative control), followed by fixation with 4% paraformaldehyde and permeabilization
737 with 0.1% Triton X-100. Cells were incubated with anti-HA and anti-puromycin antibodies,
738 followed by Duallink proximal ligation assay (PLA) as described in manufacturers protocol
739 (Sigma). For imaging, cells in mid-to-late telophase were randomly picked using following
740 criteria: (1) cells had a clearly identifiable MB as determined by GFP-MKLP1 signal; (2) cells
741 had fully reformed round nuclei; (3) cell bodies were flattened; (4) daughter cells were
742 connected by extended intercellular bridge of at least 2 μm in length.
743
744 *smiFISH probe design*
745 The smiFISH protocol was adopted from Tsanov *et al*[27]. Briefly, probes were designed by
746 inputting the gene sequences (CHMP4B, NET1, TSG101) into the Oligostan software
747 (Supplemental Table 4). smiFISH probes then had a Y flap
748 (TTACACTCGGACCTCGTCGACATGCATT) added in order to have a location where we can
749 hybridize the fluorescent molecules to the probe. The sequences can be found in Supplemental
750 Table 4. The fluorescent probe was designed by taking the reverse complement of the Y flap
751 (AATGCATGTCGACGAGGTCCGAGTGTAA) and adding Alexa488, Alexa594, or Cy3 to both
752 ends.
753
754 *smFISH probe design*
755 smFISH probes for Firefly luciferase were obtained from Biosearch Technologies. The probes
756 were labeled with Quasar 570 dye. The sequences of these probes are proprietary.
757
758
759 *smiFISH/smFISH visualization*
760 HeLa cells were plated on collagen coated coverslips and allowed to grow to 70-75%
761 confluency. The media was aspirated, and cells were washed once with 1x PBS. For Halo-tag
762 visualization, HaloTag Oregon Green Ligand was added 4-6 hours prior to fixing cells. Cells

763 were fixed in 1% PFA for 10 min at room temperature, then washed twice with 1x PBS. Cells
764 were permeabilized with 0.1% TX-100 for 5 min at room temperature. For Halo-tag visualization,
765 cells were not permeabilized to preserve Halo-tag fluorescence. The cells were washed with
766 Wash Buffer A (Stellaris) at room temperature for 5 min. In the meantime, the CHMP4B probes
767 and Y flap was hybridized using the protocol from Tsanov *et al*[27]. For smFISH, this hybridization
768 was not necessary. 2µl of the probe/flap hybridization product (0.833µM) or smFISH probe was
769 added to 100µl of smFISH hybridization buffer (Biosearch Technologies). A hybridization
770 chamber was prepared using an empty 15cm cell culture plate, wrapped in tinfoil with wet paper
771 towels surrounding the rim on the inside and parafilm covering the bottom of the plate. 100µl of
772 the probe-containing hybridization solution was added to the parafilm. The coverslip was then
773 placed on top of this droplet of hybridization buffer with the cell side down. The hybridization
774 chamber with the coverslips was incubated at 37°C overnight. On the following day, the glass
775 coverslips were transferred to a fresh 6-well plate with the cell side up and incubated with Wash
776 Buffer A (Biosearch Technologies) and Hoechst stain (1:2000, AnaSpec) at room temperature in
777 the dark for 30 min. Hoechst stain was washed with Wash Buffer B (Biosearch Technologies) at
778 room temperature in the dark for 5 min. Coverslips were then mounted onto slides with
779 Fluoromount G (Southern Biotech) and sealed with clear nail polish. Slides were imaged using
780 an inverted Axiovert 200M microscope (Zeiss) with a 63X oil immersion lens and QE charge-
781 coupled device camera (Sensicam).
782
783 *smFISH particle counting*
784 ImageJ was used to count the total number of smiFISH particles. First, the channels were
785 separated, and an outline of the cell was drawn using the freehand tool in the smFISH channel.
786 Next, a threshold was set using a control cell. The threshold set with the control cell was used
787 for all cells after that. Finally, the particles were analyzed to get the total number of particles in
788 each cell.
789
790 FISH-quant
791 FISH-quant was used to quantify midbody or intercellular bridge enrichment of smFISH spots as
792 previously described[50]. Briefly, outlines were drawn in the FITC channel visualizing Halo-
793 MKLP1. Four outlines were drawn per dividing cell: 2 cells on each side of the bridge, the
794 intercellular bridge, and the midbody marked by Halo-MKLP1. Prior to quantification, identified
795 smFISH spots were thresholded for intensity, sphericity, amplitude and position. Reporter
796 enrichment was quantified by the total number of spots in the intercellular bridge or midbody of
797 cells over total number of spots in the whole cell normalized to the control.
798
799 *Puromycin treatment*
800 HeLa cells were plated on collagen-coated coverslips and allowed to grow to 70-75%
801 confluency. At this time, cells were exposed to 25µM puromycin and incubated at 37°C for 1 h.
802 Cells were then fixed, stained, and imaged as previously described.
803
804 *Anti-Puromycin labeling*
805 HeLa cells were plated on collagen-coated coverslips and allowed to grow to 70-75%
806 confluency. At this time, the cells were either treated with DMSO (volume equal to that of the
807 other treatments) for 40 min at 37°C, 50µM cycloheximide for 40 min plus the last 10 min with
808 25µM puromycin at 37°C, or only 25µM puromycin for 10min at 37°C. Cells were then fixed,
809 stained, and imaged as previously described.
810
811 *Puromycin Wash-Out Assay*
812 HeLa cells were plated on collagen-coated coverslips and allowed to grow to 70-75%
813 confluency. At this time, the cells were either untreated, treated with 25µM puromycin at 37°C

814 for 1 h, treated with 25μM puromycin at 37°C for 1 h, washed with 1x PBS and allowed to
815 recover for 5 min in complete media at 37°C, or treated with 25μM puromycin at 37°C for 1 h,
816 washed with 1x PBS and allowed to recover for 10 min in complete media at 37°C. Cells were
817 then fixed, stained, and imaged as previously described.
818
819 *Generation of doxycycline-inducible constructs*
820 Due to the GC rich nature, we were unable to PCR the full-length 3'-UTR. Therefore, we used
821 Twist Bioscience to generate a modified sequence that we could use for a template
822 (TGGGGTCCAGCGCTGGCTGGGCCCAGACAGACTGTGGTGGCCTGCGCAGCGAGCAGGC
823 GTGTGCGTGTGTGGGGCAGGCAGGATGTGGTGCAGGCAGGTTCCATCGCTTTCGACTCTC
824 ACTCCAAAGCAGTAGGGCCGCGTTGCTGCTCACTCTCTGCATAGCATGGTCTGGAAGTGT
825 GCTGTTTATAATGTTGAATTTCTGTAAAATAAACTGTATTTGCAAATCCAACATTGAGCTTCT
826 GGACTACGCTGACTCCACTGCTGAATCCTCAATGGAAAGGGTCGACTGGTTGCAGTTGAA
827 ATGACCTGAAATGTAGCCTCTGTCCTTGTAAGTCAGTTGACTTGCCGCACATCTCTTTGTGT
828 ACTTGTACGGTACTGGCAGAAAAGTCATTTTTCAAAAGCCATAGGCTTTTCCTTGCCCTTAG
829 CTGTAATAATGCATCTGATTTTGATTTCCTCCAGAGCTGTGTTTCTGTCCATCACCTGTGTA
830 TTGGCCCTGTGTTTACCACTCTGGCCCACTCCTCACCCCCTTGCTCCCCTGGTCTTCTGGA
831 GTTTGTGACATTGATTTGAAATGGATGGTGTTCTCTTGAGAGCAAGTGAGATTGTTAGAATT
832 AAGTTCCAACTATACAGTTTTCTAACATAGCTATAAGGTCCTTGTTGCTGTTTGTGATAACTG
833 ATAGATAACTCATTGGAAACGTGCATACATTTATATTCAGATGAAATTATGGTTTGCACTGTC
834 TATTAAATATCTCGATTAATTTTCATA). This sequence maintains the GA rich motifs thought to
835 be important for translocation.
836
837 To insert the various doxycycline-inducible constructs into the backbone (pRD-RIPE), we used
838 the NEBuilder Assembly tool and followed the programs direction to generate forward and
839 reverse primers for generating PCR products for the insert and the backbone (listed in the
840 Supplemental Table 5). Q5 High-Fidelity 2x Master Mix (New England Biolabs) was used to
841 perform the PCR according to the manufacturer's protocol. NEBuilder HiFi DNA Assembly
842 Master Mix was used to assemble the inserts and backbones according to the manufacturer's
843 protocol and transformed into XL10-Gold competent cells (Agilent). Bacteria containing the
844 constructs were then grown overnight at 37°C and the DNA was extracted using the Zyppy
845 Plasmid Miniprep Kit (Zymo Research) according to the manufacturer's protocol.
846
847 For the RFP-3′UTR, RFP-CHMP4B-3′UTR were generated as described above and then using
848 the NEBuilder system, the CHMP4B coding region was removed by PCR and re-assembled to
849 get RFP-3′UTR construct. For the RFP-CHMP4B No Start, the RFP-CHMP4B was generated as
850 described above and then using the NEBuilder system, the start codon was removed by PCR
851 and re-assembled to get the RFP-CHMP4B No Start construct.
852
853
854 *Transfection of doxycycline-inducible constructs*
855 HeLa acceptor lines containing a HeLa LoxP site were plated in a 6-well plate and allowed to
856 grow to 60% confluency. Cells were then co-transfected with a pRD-RIPE construct containing a
857 gene of interest, along with a Cre-encoding plasmid (pBT140) at a 0.5%-10% wt/wt ratio. To
858 transfect 1 well in a 6-well plate, a total of 2.1μg of DNA was mixed with 5.625μL of
859 Lipofectamine 2000 (Thermo Fisher Scientific) and 246μL of Opti-MEM (Invitrogen) following the
860 manufacturer's protocol. Cells were incubated with the transfection mixture overnight, the
861 medium was changed, and the incubation continued for another 24 h before adding puromycin.
862 We used a two-step selection protocol, beginning with half of the maximal puromycin
863 concentration (0.5μg/mL) for the first 48 h of selection, followed by the maximal puromycin
864 concentration (1μg/mL) for several days until the puromycin-sensitive cells were eliminated. The

865 cultures were incubated until the appearance of visible puromycin-resistant colonies, which
866 were then pooled together and expanded.
867
868 *Induction of doxycycline-inducible cell lines*
869 Cells containing a doxycycline-inducible gene of interest were subject to 2µg/mL of
870 doxycycline and allowed to grow for 48 h unless otherwise stated. After 48 h, the cells were
871 either fixed on collagen-coated coverslips for immunofluorescence, lysed for western blot
872 analysis, or the media was collected for MBsome isolation.
873
874 *Cell lysis and western blot analysis*
875 Cells were lysed on ice in a buffer containing 20 mM Hepes, pH 7.4, 150 mM NaCl, 1% Triton
876 X-100, and 1 mM PMSF. After 30 min, lysates were clarified at 15,000 g
877 in a prechilled microcentrifuge. Supernatants were collected and analyzed via Bradford assay
878 (5000006; Bio-Rad Protein Assay). 50-µg lysate samples were prepared (unless otherwise
879 stated) in 4× SDS loading dye, boiled for 5 min at 95°C, and separated via SDS-PAGE. Gels
880 were transferred onto 0.45-µm polyvinylidene difluoride membrane (IPFL00010), followed by
881 blocking for 30 min in Intercept Blocking Buffer diluted in TBST 1:3 (927-60001). Primary
882 antibodies (made in diluted Intercept Blocking Buffer) were incubated overnight at 4°C. The next
883 day, blots were washed in TBST followed by incubation with IRDye fluorescent secondary
884 antibody (diluted Intercept Blocking Buffer) for 30 min at room temperature. Blots were washed
885 once again with TBST before final imaging on a Li-Cor Odyssey CLx.
886
887 *Statistical analysis*
888 All statistical analyses were performed using GraphPad Prism Software (GraphPad, San Diego,
889 CA). A Student's t-test was used to determine significance unless otherwise noted. Error bars
890 represent standard deviation unless otherwise noted. For all immunofluorescence experiments,
891 at least 20 randomly chosen image fields from at least 3 separate experiments were used for
892 data collection. For quantitative immunofluorescence analysis, the same exposure was used for
893 all images in that experiment and was quantified using Intelligent Imaging Innovations software
894 (Denver, CO, USA). For western blot experiments, 3 separate experimental examples were
895 used for data collection. For quantitative western blot analysis, Image Studio V5.2 software (LI-
896 COR, Lincoln, NE) was used to collect intensities.
897
898
899 **Acknowledgements**
900 We would like to thank the University of Colorado Anschutz Medical Campus Genomics Facility
901 and Novogene for performing the RNAseq and the RNA Biosciences Initiative (RBI) for help in
902 analyzing the RNAseq data and Migle Prekeryte for critically reading and editing the manuscript.
903 This work was supported by NIGMS grant R01-GM143774 to RP, R35-GM133385 to JMT, and
904 RBI Pilot Grant to RP and JMT. Additionally, some of the work was also supported by Diversity
905 Supplement GM143774-02S1 to KV.
906
907 **Figure Legends**
908 **Figure 1. MBsomes contain a distinct subset of mRNAs.**
909 (A) Schematic representing MB formation and MBsome release into the media. MBsomes from
910 the media were isolated for RNAseq analysis presented in this study.
911 (B) Principal component analysis representing the difference between the 3 control and the 3
912 MB RNAseq datasets.
913 (C) Correlation analysis representing the correlation between the various control and MB
914 RNAseq datasets.

(D) Volcano plot showing the significantly depleted (pink) and significantly enriched (purple) mRNAs found within MBsomes from 3 RNAseq datasets.

Figure 2. MBsomes are enriched in mRNAs encoding proteins that regulate translation and cell cycle.
(A) The Gene Ontology (GO) pathway analysis tool was used to determine the pathways associated with the enriched MB-associated mRNAs.
(B) MB enrichment of mRNAs encoding known abscission regulators. Data shown presents means and standard deviations derived from three separate RNAseq analyses. Dashed line marks the mRNA levels present in the whole cell transcriptome.
(C) Whole cell or MBsome-associated mRNAs were isolated from GFP-MKLP1-expressing HeLa cell line. The cDNA was subject to RT-qPCR using TSG101, CHMP4B, CHMP2A, CHMP3, CHMP6, or GAPDH (control) specific primers and represented as normalized values. Statistical analysis is represented with a p-value.
(D) Schematic representing key regulators of abscission and how they relate to each other in the intercellular bridge.

Figure 3. Midbodies contain molecular machinery required for protein translation.
(A) GFP-MKLP1 expressing HeLa cells were either mock treated or treated with CHMP4B siRNA for 72 h and subjected to staining with smFISH probes against CHMP4B. Arrows in the inset points to CHMP4B mRNA particles. The cell outline is marked in yellow with the asterisks marking the MB. The black dashed square represents the region of the image used for the inset.
(B) ImageJ was used to count the number of CHMP4B smFISH particles in the mock or CHMP4B siRNA treated cells. Each dot represents a single cell.
(C) The Database for Annotation, Visualization, and Integrated Discovery (DAVID) was used to determine that ribosomal proteins and translation initiation factors are enriched in all 3 published MB proteomes.
(D) HeLa cells were fixed and subjected to immunostaining with anti-acetylated-tubulin (red) and anti-RPL3 (green) antibodies. The line used for the line intensity graphs is marked in yellow and the asterisks mark the MB. The white dashed square represents the region of the image used for the inset.
(E-F) Line intensity graphs representing the intensity of acetylated-tubulin (red) and RPL3 (green). Negative control was derived from samples that were treated with secondary antibodies but without anti-RPL3 antibodies.

Figure 4. Active protein translation occurs in the midbody.
(A) Schematic representing the 3 treatment conditions and times used for the experiments represented in panels (B-E).
(B) HeLa cells were treated with either DMSO, CHX+Puromycin, or Puromycin and subjected to immunostaining with anti-acetylated-tubulin and anti-puromycin antibodies. The asterisks mark the MB, and the white dashed square represents the region of the image used for the inset.
(C-D) 3i imaging software was used to measure the anti-puromycin intensity/micron^2 in the intercellular bridge of 60 cells from 3 separate experiments (C; each dot represents one cell). Statistical analysis was done on means and standard deviations derived from the 3 individual experiments (D). Each experiment is represented by a different shade of color and is the mean derived from all cells analyzed in that particular experiment. Statistical analysis is represented with a p-value.
(E) HeLa cells were treated with either DMSO, CHX+Puromycin, or Puromycin and subjected to immunostaining with anti-puromycin (to mark the puromycylated peptides) and anti-CHMP4B antibodies. The line used for the line intensity graphs is marked in yellow and the asterisks mark the MB. The white dashed square represents the region of the image used for the inset.

(F-H) Line intensity graphs representing the intensity of Puromycin (red) and CHMP4B (green) signals after DMSO (F), CHX+Puromycin (G), or Puromycin (H) treatments.

Figure 5. Inhibition of translation inhibits CHMP4B accumulation at the midbody.
(A) HeLa cells were either untreated or treated with puromycin for 1 h and subjected to immunostaining with anti-acetylated-tubulin and anti-CHMP4B antibodies. The asterisks mark the MB, and the white dashed square represents the region of the image used for the inset.
(B-C) Shown data represents CHMP4B intensity/micron^2 in the intercellular bridge of 60 cells from 3 separate experiments. Panel B shows distributions derived from individual cells (each dot represents a single cell). Statistical analysis in panel C was done on the means and standard deviations derived from the 3 individual experiments where experimental means were calculated by averaging values from all the cells from each experiment. Each experiment is represented by a different shade of color. Statistical analysis is represented with a p-value.
(D-E) Shown data represents CHMP4B intensity/micron^2 in the cell body of 60 cells from 3 separate experiments. Panel D shows distributions derived from individual cells (each dot represents a single cell). Statistical analysis in panel E was done on the means, and standard deviations were derived from the 3 individual experiments where experimental means were calculated by averaging values from all the cells from each experiment. Each experiment is represented by a different shade of color. Statistical analysis is represented with a p-value.
(F) HeLa cells were either untreated or treated with puromycin for 1 h and subjected to immunostaining with anti-acetylated-tubulin and anti-CEP55 antibodies. The asterisks mark the MB, and the white dashed square represents the region of the image used for the inset.
(G-H) Shown data represents CEP55 intensity/micron^2 in the intercellular bridge of 60 cells from 3 separate experiments. Panel G shows distributions derived from individual cells (each dot represents a single cell). Statistical analysis in panel H was done on the means, and standard deviations were derived from the 3 individual experiments where experimental means were calculated by averaging values from all the cells from each experiment. Each experiment is represented by a different shade of color. Statistical analysis is represented with a p-value.
(I-J) Shown data represents CEP55 intensity/micron^2 in the cell body of 60 cells from 3 separate experiments. Panel I show the distributions derived from individual cells (each dot represents a single cell). Statistical analysis in panel J was done on the means, and standard deviations were derived from the 3 individual experiments where experimental means were calculated by averaging values from all the cells from each experiment. Each experiment is represented by a different shade of color. Statistical analysis is represented with a p-value.
(K) HeLa cells after puromycin treatment were fixed and stained with anti-acetylated tubulin antibodies. The percentage of cells in telophase was then counted. Shown data are the means and standard deviations derived from three independent experiments. Statistical analysis is represented with a p-value.
(L) HeLa cells after puromycin treatment were fixed and stained with anti-acetylated tubulin antibodies. The percentage of cells that just completed abscission was then counted. Shown data are the means and standard deviations derived from three independent experiments. Statistical analysis is represented with a p-value.
(M) HeLa cells were either untreated, treated with puromycin, CEP55 siRNA, or CEP55 siRNA plus puromycin and subjected to immunostaining anti-acetylated-tubulin and anti-CHMP4B antibodies. The asterisks mark the MB, and the white dashed square represents the region of the image used for the inset.
(N-O) Shown data represents CHMP4B intensity/micron^2 in intracellular of 60 cells from 3 separate experiments. Panel N shows distributions derived from individual cells (each dot represents a single cell). Statistical analysis in panel O was done on the means, and standard deviations were derived from the 3 individual experiments where experimental means were

1016 calculated by averaging values from all the cells from each experiment. Each experiment is
1017 represented by a different shade of color. Statistical analysis is represented with a p-value.
1018
1019 **Figure 6. Puromycin wash-out leads to fast recovery of CHMP4B levels in MB.**
1020 (A) HeLa cells were either untreated or treated for 1 h with puromycin. Cells were then washed
1021 and incubated with complete media for either 5 min or 10 min. Cells were then fixed and
1022 subjected to immunostaining with anti-acetylated-tubulin and anti-CHMP4B antibodies. The
1023 asterisks mark the MB, and the white dashed square represents the region of the image used
1024 for the inset.
1025 (B-C) Shown data represents CHMP4B intensity/micron^2 in the intercellular bridge of 60 cells
1026 from 3 separate experiments. Panel B shows distributions derived from individual cells (each dot
1027 represents a single cell). Statistical analysis in panel C was done on the means, and standard
1028 deviations were derived from the 3 individual experiments where experimental means were
1029 calculated by averaging values from all the cells from each experiment. Each experiment is
1030 represented by a different shade of color. Statistical analysis is represented with a p-value.
1031 (D-E) Shown data represents CHMP4B intensity/micron^2 in the cell body of 60 cells from 3
1032 separate experiments. Panel D shows distributions derived from individual cells (each dot
1033 represents a single cell). Statistical analysis in panel E was done on the means, and standard
1034 deviations were derived from the 3 individual experiments where experimental means were
1035 calculated by averaging values from all the cells from each experiment. Each experiment is
1036 represented by a different shade of color. Statistical analysis is represented with a p-value.
1037 (F-G) HeLa cells that were untreated or treated for 1 h with puromycin. Cells were then washed
1038 and incubated with media for an additional 5 or 10 minutes. Cells were then fixed and stained
1039 with anti-acetylated-tubulin antibodies. The percentage of cells in either telophase (F) or just
1040 after abscission (G) was then counted. Shown data are means and standard deviations derived
1041 from three independent experiments. Statistical analysis is represented with a p-value.
1042
1043
1044 **Figure 7. The 3′ UTR of CHMP4B is important for protein accumulation and mRNA**
1045 **translocation.**
1046 (A) HeLa cells expressing various RFP-tagged dox-inducible constructs were incubated with
1047 2µg/mL doxycycline for 48 h and then subjected to immunostaining with anti-acetylated-tubulin.
1048 The asterisks mark the MB, and the white dashed square represents the region of the image
1049 used for the inset.
1050 (B-C) Ratio between RFP fluorescence in the intracellular bridge and cell body was calculated
1051 from 60 randomly chosen cells in telophase. Panel B shows distributions derived from individual
1052 cells (each dot represents a single cell). Statistical analysis in panel C was done on the means,
1053 and standard deviations were derived from the 3 individual experiments where experimental
1054 means were calculated by averaging values from all the cells from each experiment. Each
1055 experiment is represented by a different shade of color. Statistical analysis is represented with a
1056 p-value.
1057 (D) HeLa cells expressing various RFP-tagged dox-inducible constructs were incubated with
1058 2µg/mL doxycycline for 48 h and then subjected to immunostaining with anti-acetylated-tubulin.
1059 The percentage of cells with multinucleation was then counted. Shown data are the means and
1060 standard deviations derived from three independent experiments. Statistical analysis is
1061 represented with a p-value.
1062 (E) HeLa cells expressing various RFP-tagged dox-inducible constructs were incubated with
1063 2µg/mL doxycycline for 48 h and then subjected to immunostaining with anti-acetylated-tubulin.
1064 The percentage of cells in telophase was then counted. Shown data are the means and

1065 standard deviations derived from three independent experiments. Statistical analysis is
1066 represented with a p-value.
1067 (F) HeLa cells expressing dox-inducible RFP-CHMP4B or RFP-CHMP4B-3'UTR constructs
1068 were incubated with 2µg/mL doxycycline for 48 h and subjected to staining with smFISH probes
1069 against CHMP4B. The cell outline is marked in yellow with the asterisks marking the MB. The
1070 black dashed square represents the region of the image used for the inset.
1071 (G) Whole cell or MB-associated mRNA was isolated from these cell lines expressing various
1072 RFP-tagged constructs and subject to RT-qPCR analysis using RFP or GAPDH (control)
1073 specific primers. RFP mRNA levels were then normalized against GAPDH mRNA and
1074 expressed as a ratio between MB and whole cell RFP mRNA levels. Statistical analysis is
1075 represented with a p-value and was done on the means and standard deviations derived from
1076 three independent experiments.
1077
1078 **Figure 8. The 3′ UTR is required for CHMP4B translation at the MB during telophase.**
1079 (A) HeLa cells were transfected with RFP-CHMP4B-3′UTR and plated on glass-bottom dishes.
1080 The accumulation of RFP-CHMP4B at the MB during telophase was then imaged using time-
1081 lapse microscopy for 120 minutes with 15 minute time-lapse. Asterisk marks the midbody
1082 (B) HeLa cells stably expressing GFP-MKLP1 were transfected with either HA-CHMP4B-3′UTR
1083 (images on the left) or HA-CHMP4B (images on the right). Cells were then fixed and incubated
1084 with anti-HA and anti-puromycin antibodies followed with proximity ligation assay (PLA).
1085 Asterisk marks the midbody. Boxes mark area shown in higher magnification insets.
1086 (C) Negative controls for PLA experiment shown in panel B. Cells in image on the left were not
1087 treated with puromycin but transfected with HA-CHMP4B-3′UTR. Cells in image on the right
1088 were treated with puromycin but not transfected with HA-CHMP4B-3′UTR. Asterisk marks the
1089 midbody.
1090 (D) Quantification of the levels of PLA signal in the midbody area. Data shown are the means
1091 and standard errors of mean. Each circle indicates the data derived from one dividing cell.
1092
1093 **Figure 9. Transcripts associated with the plus-ends of microtubules are enriched in the**
1094 **MB transcriptome.**
1095 (A) Comparison of MB-associated mRNA with RNAs enriched in neuronal projections of mouse
1096 neuronal cells. Genes were binned into MB-localized RNAs and non-MB-localized RNAs.
1097 Neurite RNA enrichment values (neurite RNA / soma RNA, log2) from previous published data
1098 were then calculated for the mouse orthologs of all genes, and the distributions of enrichment
1099 values were compared between bins. P values were calculated using a Wilcoxon rank-sum test.
1100 (B) As in A, genes were binned according to their MB RNA enrichment. Using a previous
1101 published comparison of the apical and basal compartments of epithelial cells, basal enrichment
1102 values (basal RNA / apical RNA, log2) were calculated for all genes, and the distributions of
1103 enrichment values were compared between bins. P values were calculated using a Wilcoxon
1104 rank-sum test.
1105 (C) *NET1* RNA enrichment in human midbodies compared to whole cells (left) and mouse
1106 neurites compared to cell bodies (right).
1107 (D) smiFISH for endogenous *NET1* mRNA localization (yellow) in cells stably expressing Halo-
1108 MKLP1 (pink). Midbody is marked with an asterisk. The box indicates the area shown in a
1109 higher magnification inset.
1110 (E) Quantification of *NET1* smiFISH. Transcript counts were quantified in the intercellular bridge
1111 and whole cell areas. For each cell, the number of counts in the intercellular bridge was
1112 normalized by the number of counts in the whole cell. The median ratio for this value across all
1113 cells for the control *TSG101* transcript was set to one. P values were calculated using a t-test.
1114 (F) As in E, except that transcript counts in the midbody and whole cell regions were compared.
1115 P values were calculated using a t-test.

1116
1117
1118 **Figure 10. *NET1* 3′ UTR localization elements are necessary and sufficient to target**
1119 **mRNA to the MB**
1120 (A) Schematic RT-qPCR-based reporter RNA approach for assaying MB RNA localization.
1121 Plasmids expressing Firefly and Renilla luciferases from a bidirectional reporter are integrated
1122 into the genome. Sequences to be tested for MB localization activity (*NET1* full length 3′ UTR,
1123 LE and LE deletion) are fused to the 3′ UTR of Firefly luciferase. Using Taqman qPCR, the ratio
1124 of Firefly to Renilla luciferase mRNA is measured in MB and whole cell samples. The ratio of
1125 these ratios (MB / WC) quantifies the MB-enrichment of the Firefly luciferase transcript. By
1126 asking how this value changes upon appending additional sequences to the Firefly luciferase
1127 RNA, the effects of these additional sequences on MB RNA enrichment can be tested.
1128 (B) Diagram of reporter constructs used to interrogate *NET1* localization activity in MBs.
1129 smFISH probes against the Firefly luciferase coding sequence are shown as red stars.
1130 (C) Localization of the reporter RNAs described in B to the MB as quantified using the strategy
1131 outlined in A. The value for the control reporter lacking additional sequence elements was set to
1132 one. P values were calculated using a t-test.
1133 (D) smFISH visualizing the reporter RNAs described in B (yellow) in cells stably expressing
1134 Halo-MKLP1 (pink). Midbody is marked with an asterisk. The box indicates the area shown in a
1135 higher magnification inset.
1136 (E) Quantification of MB-localized *Net1* UTR-containing reporter transcripts visualized in D. In all
1137 samples, reporter transcript counts in intercellular bridges and whole cells were quantified and
1138 the ratio of counts between the two locations is reported. These ratios were normalized by
1139 setting the value for the control reporter transcript lacking 3′ UTR additions to one. P values
1140 were calculated using a t-test.
1141
1142 **Supplemental Figure 1.**
1143 (A) Comparison of MB-Associated mRNA with RNA contents of HeLa cells in G2/M and G1 cell
1144 cycle phases. (B) Comparison of MB-Associated mRNA with RNA contents of HeLa cells in S
1145 and G1 cell cycle phases. (C) Comparison of MB-Associated mRNA with spindle-associated
1146 RNA.
1147
1148 **Supplemental Figure 2.**
1149 (A-B) GFP-MKLP1 expressing HeLa cells were either mock treated or treated with CHMP4B (A)
1150 or CEP55 (B) siRNAs. Cells were then incubated for 72 h, followed by mRNA isolation and RT-
1151 qPCR analysis using CHMP4B, CEP55, and GAPDH (control) specific primers. Data shown are
1152 the CHMP4B or CEP55 mRNA levels normalized against GAPDH mRNA.
1153 (C-D) GFP-MKLP1 expressing HeLa cells were either mock treated (top two panels) or treated
1154 with puromycin for 1 h (bottom two panels) and subject to staining with smFISH probes against
1155 CHMP4B mRNA. CHMP4B mRNA particles are marked by the arrows in the inset and the black
1156 dashed square represents the region of the image used for the inset (C). The number of cells
1157 with CHMP4B smFISH signal was then counted. The data shown in panel D represents the
1158 means and standard deviations derived from three independent experiments.
1159 (E) GFP-MKLP1 expressing HeLa cells were either mock treated or treated with CEP55 siRNA
1160 for 72 hours. Cells were then fixed and subjected to staining with smFISH probes against
1161 CHMP4B mRNA. The number of cells with CHMP4B smFISH signal in the MB were then
1162 counted and expressed as means and standard deviations derived from three independent
1163 experiments.
1164
1165 **Supplemental Figure 3. The effect of puromycin treatment on CHMP4B targeting to the**
1166 **MB in synchronized cells**

(A) Synchronization and puromycin treatment schematics
(B-C) Synchronized HeLa cells were incubated for 90 minutes in the presence or absence of puromycin (during last 30 minutes of incubation). Cells were then foxed and stained with anti-CHMP4B antibodies (red). Asterisk marks the midbody. Panel C shows quantification of CHMP4B localization in the midbody. Data shown are the means and standard deviations. Dots represents localization in individual cells.

Supplemental Figure 4.
(A-B) HeLa cells were fixed and subjected to immunostaining using anti-acetylated-tubulin. The panel A represents a cell in telophase. Panel B represents a cell that had just undergone abscission (see arrow). The lines used for the line intensity graphs are marked in yellow, and the white dashed square represents the region of the image used for the inset.
(C-D) Line intensity graphs representing the intensity of acetylated-tubulin in telophase and abscission cells. The abscission site is marked by an arrow (D).
(E-F) Telophase HeLa cells stably expressing GFP-MKLP1 were analyzed by time-lapse microscopy. Cells were imaged for 120 minutes with 15 minute time-lapse.

Supplemental Figure 5. Characterization of HeLa LoxP cells expressing doxycycline-inducible RFP-tagged constructs.
(A) HeLa LoxP cells expressing various RFP-tagged dox-inducible constructs cells were untreated (-Dox) or treated with 2µg/mL doxycycline for 48 h (+Dox). RFP was visualized by fluorescent microscopy to test for dox-dependent expression. The white dashed square represents the region of the image used for the inset.
(B-D) HeLa LoxP cells expressing various RFP-tagged dox-inducible constructs cells were untreated (-Dox) or treated with 2µg/mL doxycycline for 48 h (+Dox). The construct expression levels were then determined by RT-qPCR using CHMP4B specific primers.
(E) HeLa LoxP cells expressing various RFP-tagged dox-inducible constructs cells were treated with 2µg/mL doxycycline for 48 h. The levels of expression among various constructs were the n compared using RT-qPCR with RFP specific primers.
(F-G) HeLa LoxP cells expressing various RFP-tagged dox-inducible constructs cells were untreated (-Dox) or treated with 2µg/mL doxycycline for 48 h (+Dox). The levels of RFP-tagged protein expressions were visualized via western blot using anti-RFP and anti-Actin (loading control) antibodies. Panel G shows Western blot quantification from 3 individual experiments. Statistical analysis is represented with a p-value.

Supplemental Figure 6.
(A) smiFISH for endogenous *NET1* mRNA localization (red) in human epithelial cells. As a nonlocalized control, transcripts encoding an exogenous Firefly luciferase are also visualized.
(B) Quantification of *NET1* RNA localization along the apicobasal axis of epithelial cells.
(C) Quantification of MB-localized *Net1* UTR-containing reporter transcripts. In all samples, reporter transcript counts in midbodies and whole cells were quantified and the ratio of counts between the two locations is reported. These ratios were normalized by setting the value for the control reporter transcript lacking 3′ UTR additions to one. P values were calculated using a t-test.

Supplemental Table 1. List of mRNAs identified in RNAseq analyses of purified MBs

Supplemental Table 2. SYBR RT-qPCR primer sequences

Supplemental Table 3. Taqman RT-qPCR primer sequences

1217
1218 **Supplemental Table 4. smiFISH probe sequences**
1219
1220 **Supplemental Table 5. Primer sequences used for cloning**
1221
1222
1223
1224 **References**

1225 1. Carlton, J. The ESCRT machinery: a cellular apparatus for sorting and scission. *Biochem*
1226 *Soc Trans* **38**, 1397-1412 (2010).
1227 2. Schoneberg, J., Lee, I.H., Iwasa, J.H. & Hurley, J.H. Reverse-topology membrane scission
1228 by the ESCRT proteins. *Nat Rev Mol Cell Biol* **18**, 5-17 (2017).
1229 3. Carlton, J.G. & Martin-Serrano, J. Parallels between cytokinesis and retroviral budding: a
1230 role for the ESCRT machinery. *Science* **316**, 1908-1912 (2007).
1231 4. Morita, E. *et al.* Human ESCRT and ALIX proteins interact with proteins of the midbody
1232 and function in cytokinesis. *EMBO J* **26**, 4215-4227 (2007).
1233 5. Carlton, J.G., Agromayor, M. & Martin-Serrano, J. Differential requirements for Alix and
1234 ESCRT-III in cytokinesis and HIV-1 release. *Proc Natl Acad Sci U S A* **105**, 10541-10546
1235 (2008).
1236 6. Guizetti, J. *et al.* Cortical constriction during abscission involves helices of ESCRT-III-
1237 dependent filaments. *Science* **331**, 1616-1620 (2011).
1238 7. Goliand, I., Nachmias, D., Gershony, O. & Elia, N. Inhibition of ESCRT-II-CHMP6
1239 interactions impedes cytokinetic abscission and leads to cell death. *Mol Biol Cell* **25**,
1240 3740-3748 (2014).
1241 8. Addi, C. *et al.* The Flemmingsome reveals an ESCRT-to-membrane coupling via
1242 ALIX/syntenin/syndecan-4 required for completion of cytokinesis. *Nat Commun* **11**, 1941
1243 (2020).
1244 9. Elia, N., Sougrat, R., Spurlin, T.A., Hurley, J.H. & Lippincott-Schwartz, J. Dynamics of
1245 endosomal sorting complex required for transport (ESCRT) machinery during cytokinesis
1246 and its role in abscission. *Proc Natl Acad Sci U S A* **108**, 4846-4851 (2011).
1247 10. Goliand, I. *et al.* Resolving ESCRT-III Spirals at the Intercellular Bridge of Dividing Cells
1248 Using 3D STORM. *Cell Rep* **24**, 1756-1764 (2018).
1249 11. Christ, L., Raiborg, C., Wenzel, E.M., Campsteijn, C. & Stenmark, H. Cellular Functions
1250 and Molecular Mechanisms of the ESCRT Membrane-Scission Machinery. *Trends*
1251 *Biochem Sci* **42**, 42-56 (2017).
1252 12. Agromayor, M. *et al.* Essential role of hIST1 in cytokinesis. *Mol Biol Cell* **20**, 1374-1387
1253 (2009).
1254 13. Christ, L. *et al.* ALIX and ESCRT-I/II function as parallel ESCRT-III recruiters in cytokinetic
1255 abscission. *J Cell Biol* **212**, 499-513 (2016).
1256 14. Morita, E. *et al.* Human ESCRT-III and VPS4 proteins are required for centrosome and
1257 spindle maintenance. *Proc Natl Acad Sci U S A* **107**, 12889-12894 (2010).
1258 15. Carlton, J.G., Caballe, A., Agromayor, M., Kloc, M. & Martin-Serrano, J. ESCRT-III governs
1259 the Aurora B-mediated abscission checkpoint through CHMP4C. *Science* **336**, 220-225
1260 (2012).

1261 16. Mierzwa, B. & Gerlich, D.W. Cytokinetic abscission: molecular mechanisms and temporal
1262 control. *Dev Cell* **31**, 525-538 (2014).
1263 17. Addi, C., Bai, J. & Echard, A. Actin, microtubule, septin and ESCRT filament remodeling
1264 during late steps of cytokinesis. *Curr Opin Cell Biol* **50**, 27-34 (2018).
1265 18. Tedeschi, A. *et al.* Cep55 promotes cytokinesis of neural progenitors but is dispensable
1266 for most mammalian cell divisions. *Nat Commun* **11**, 1746 (2020).
1267 19. Dionne, L.K., Wang, X.J. & Prekeris, R. Midbody: from cellular junk to regulator of cell
1268 polarity and cell fate. *Curr Opin Cell Biol* **35**, 51-58 (2015).
1269 20. Kuo, T.C. *et al.* Midbody accumulation through evasion of autophagy contributes to
1270 cellular reprogramming and tumorigenicity. *Nat Cell Biol* **13**, 1214-1223 (2011).
1271 21. Crowell, E.F., Gaffuri, A.L., Gayraud-Morel, B., Tajbakhsh, S. & Echard, A. Engulfment of
1272 the midbody remnant after cytokinesis in mammalian cells. *J Cell Sci* **127**, 3840-3851
1273 (2014).
1274 22. Chen, C.T., Ettinger, A.W., Huttner, W.B. & Doxsey, S.J. Resurrecting remnants: the lives
1275 of post-mitotic midbodies. *Trends Cell Biol* **23**, 118-128 (2013).
1276 23. Peterman, E. *et al.* The post-abscission midbody is an intracellular signaling organelle
1277 that regulates cell proliferation. *Nat Commun* **10**, 3181 (2019).
1278 24. Rai, A. *et al.* Secreted midbody remnants are a class of extracellular vesicles molecularly
1279 distinct from exosomes and microparticles. *Commun Biol* **4**, 400 (2021).
1280 25. Skop, A.R., Liu, H., Yates, J., 3rd, Meyer, B.J. & Heald, R. Dissection of the mammalian
1281 midbody proteome reveals conserved cytokinesis mechanisms. *Science* **305**, 61-66
1282 (2004).
1283 26. Peterman, E. & Prekeris, R. Understanding post-mitotic roles of the midbody during cell
1284 differentiation and polarization. *Methods Cell Biol* **137**, 173-186 (2017).
1285 27. Tsanov, N. *et al.* smiFISH and FISH-quant - a flexible single RNA detection approach with
1286 super-resolution capability. *Nucleic Acids Res* **44**, e165 (2016).
1287 28. Holt, C.E. & Bullock, S.L. Subcellular mRNA localization in animal cells and why it
1288 matters. *Science* **326**, 1212-1216 (2009).
1289 29. Khandelia, P., Yap, K. & Makeyev, E.V. Streamlined platform for short hairpin RNA
1290 interference and transgenesis in cultured mammalian cells. *Proc Natl Acad Sci U S A* **108**,
1291 12799-12804 (2011).
1292 30. D'Avino, P.P. & Capalbo, L. Regulation of midbody formation and function by mitotic
1293 kinases. *Semin Cell Dev Biol* **53**, 57-63 (2016).
1294 31. Antanaviciute, I., Gibieza, P., Prekeris, R. & Skeberdis, V.A. Midbody: From the Regulator
1295 of Cytokinesis to Postmitotic Signaling Organelle. *Medicina (Kaunas)* **54** (2018).
1296 32. Peterman, E. & Prekeris, R. The postmitotic midbody: Regulating polarity, stemness, and
1297 proliferation. *J Cell Biol* **218**, 3903-3911 (2019).
1298 33. Steigemann, P. & Gerlich, D.W. Cytokinetic abscission: cellular dynamics at the midbody.
1299 *Trends Cell Biol* **19**, 606-616 (2009).
1300 34. Farmer, T. & Prekeris, R. New signaling kid on the block: the role of the postmitotic
1301 midbody in polarity, stemness, and proliferation. *Mol Biol Cell* **33** (2022).
1302 35. Schiel, J.A. *et al.* Endocytic membrane fusion and buckling-induced microtubule severing
1303 mediate cell abscission. *J Cell Sci* **124**, 1411-1424 (2011).

1304 36. Elad, N., Abramovitch, S., Sabanay, H. & Medalia, O. Microtubule organization in the
1305 final stages of cytokinesis as revealed by cryo-electron tomography. *J Cell Sci* **124**, 207-
1306 215 (2011).
1307 37. Costa, G., Bradbury, J.J., Tarannum, N. & Herbert, S.P. RAB13 mRNA
1308 compartmentalisation spatially orients tissue morphogenesis. *EMBO J* **39**, e106003
1309 (2020).
1310 38. Moissoglu, K. *et al.* RNA localization and co-translational interactions control RAB13
1311 GTPase function and cell migration. *EMBO J* **39**, e104958 (2020).
1312 39. Arora, A. *et al.* High-throughput identification of RNA localization elements in neuronal
1313 cells. *Nucleic Acids Res* (2022).
1314 40. Goering, R., Arora, A. & Taliaferro, J.M. RNA localization mechanisms transcend cell
1315 morphology. . *Elife* **12**, e80040 (2023).
1316 41. Montagne, C. & Gonzalez-Gaitan, M. Sara endosomes and the asymmetric division of
1317 intestinal stem cells. *Development* **141**, 2014-2023 (2014).
1318 42. Patro, R., Duggal, G., Love, M.I., Irizarry, R.A. & Kingsford, C. Salmon provides fast and
1319 bias-aware quantification of transcript expression. *Nat Methods* **14**, 417-419 (2017).
1320 43. Bostrom, J., Sramkova, Z., Salasova, A., Johard, H., Mahdessian, D., Fedr, R., Marks, C.,
1321 Medalova, J., Soucek, K., Lundberg, E., Linnarsson, S., Bryja, V., Sekyrova, P., Altun, M.,
1322 and Andang, M. Cpmparative cell cycle transctiptomics reveals synchronization of
1323 developmental transcription factor networks in cancer cells. *Plos One* **12**, e0188772
1324 (2017)
1325 44. Hassine, S., Bonnet-Magnaval, F., Bouvrette, L.P., Doran, B., Ghram, M., Lecuyer, E., and
1326 DesGroseillers, L. Staufen1 localizes to the mitotic spindle and controls the localization
1327 of RNA populations to the spindle. *J Cell Sci* **133**, jcs247155 (2020)
1328 45. Schiel, J.A., Simon, G.C., Zaharis, C., Weisz, J., Castle, D., Wu, C.C., and Prekeris, R. FIP3-
1329 endosome-dependent formation of the secondary ingression mediates ESCRT-III
1330 recruitment during cytokinesis. *Nat Cell Bio* **10**, 1068-1079 (2012)
1331 46. Goering, R., Hudish, L.I., Guzman, B.B., Raj, N., Bassell, G.J., Russ, H.A., Dominguez, D.,
1332 and Taliaferro, J.M. FMRP promotes RNA localization to neuronal projections through
1333 interactions between its RGG domain and G-quadruplex RNA sequences. *Elife* **9**, e52621
1334 (2020)
1335 47. Arora, A., Castro-Gutierrez, R., Moffatt, C., Eletto, D., Becker, R., Brown, M., Moor, A.E.,
1336 Russ, H.A., and Taliaferro, J.M. High-throughput identification of RNA localization
1337 elements in neuronal cells. *Nucleic Acids Res* **50**, 10626-10642 (2022)
1338 48. Norris, M.L. and Mendell, J.T. Localization of Kif1C mRNA to cell protrusions dictates
1339 binding partner specifically of the encoded protein. Genes Dev 37, 191-203 (2023)
1340 49. Love, M.I., Huber, W., and Anders, S. Moderated estimation of fold change and
1341 dispersion for RNA-seq data with DESeq2. Genome Biol 15, 550 (2014)
1342 50. Arora, A., Goering, R., Velez, P.T., and Taliaferro, J.M. Visualization and quantification of
1343 subcellular RNA localization using single-molecule RNA fluorescence in situ
1344 hybridization. *Methods Mol Biol* **2404**, 247-266 (2022)
1345

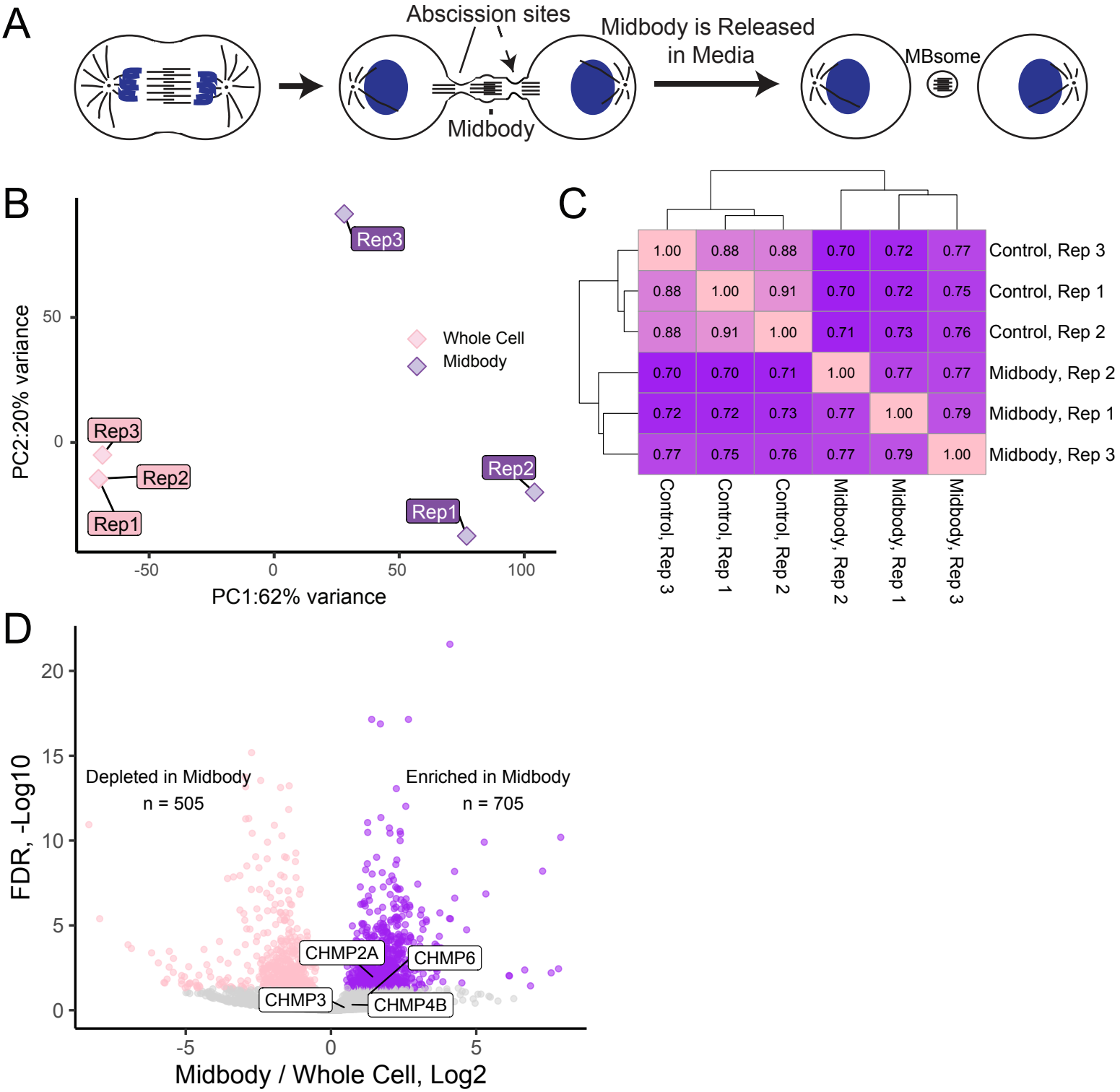
A
Abscission sites
Midbody is Released in Media
MBsome
Midbody
B
Rep3
Rep2
Rep1
Whole Cell
Midbody
PC2:20% variance
PC1:62% variance
C
Control, Rep 3
Control, Rep 1
Control, Rep 2
Midbody, Rep 2
Midbody, Rep 1
Midbody, Rep 3
D
Depleted in Midbody
n = 505
Enriched in Midbody
n = 705
CHMP2A
CHMP6
CHMP3
CHMP4B
FDR, -Log10
Midbody / Whole Cell, Log2

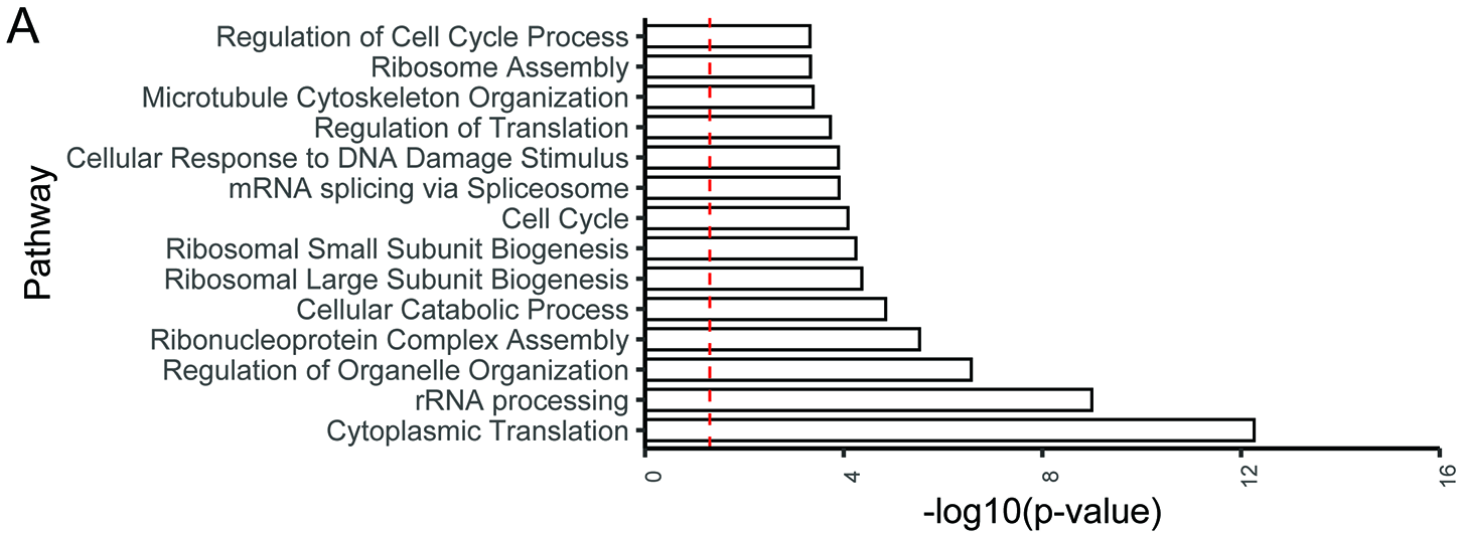
A
Pathway
Regulation of Cell Cycle Process
Ribosome Assembly
Microtubule Cytoskeleton Organization
Regulation of Translation
Cellular Response to DNA Damage Stimulus
mRNA splicing via Spliceosome
Cell Cycle
Ribosomal Small Subunit Biogenesis
Ribosomal Large Subunit Biogenesis
Cellular Catabolic Process
Ribonucleoprotein Complex Assembly
Regulation of Organelle Organization
rRNA processing
Cytoplasmic Translation
0
4
8
12
16
-log10(p-value)

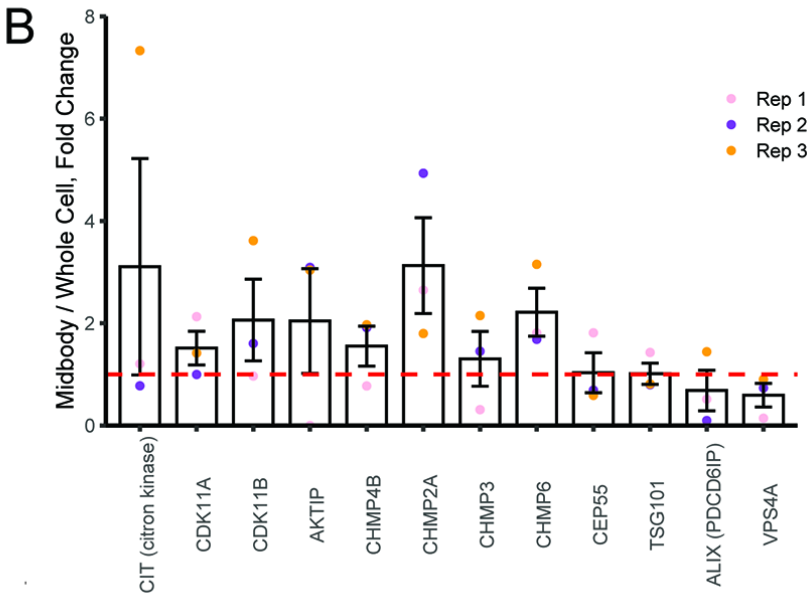
B
Midbody / Whole Cell, Fold Change
0
2
4
6
8
Rep 1
Rep 2
Rep 3
CIT (citron kinase)
CDK11A
CDK11B
AKTIP
CHMP4B
CHMP2A
CHMP3
CHMP6
CEP55
TSG101
ALIX (PDCD6IP)
VPS4A

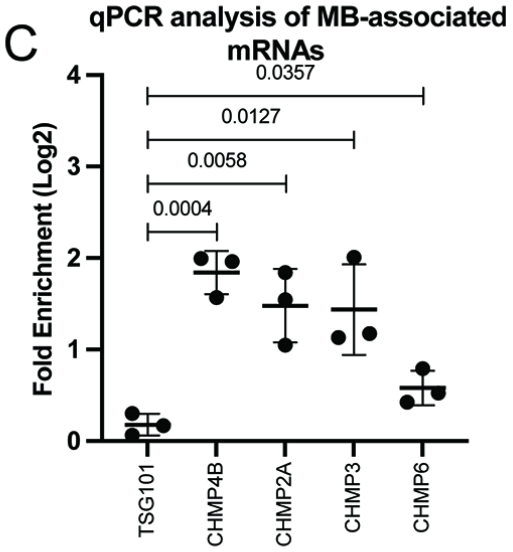
C
qPCR analysis of MB-associated mRNAs
Fold Enrichment (Log2)
0
1
2
3
4
0.0357
0.0127
0.0058
0.0004
TSG101
CHMP4B
CHMP2A
CHMP3
CHMP6

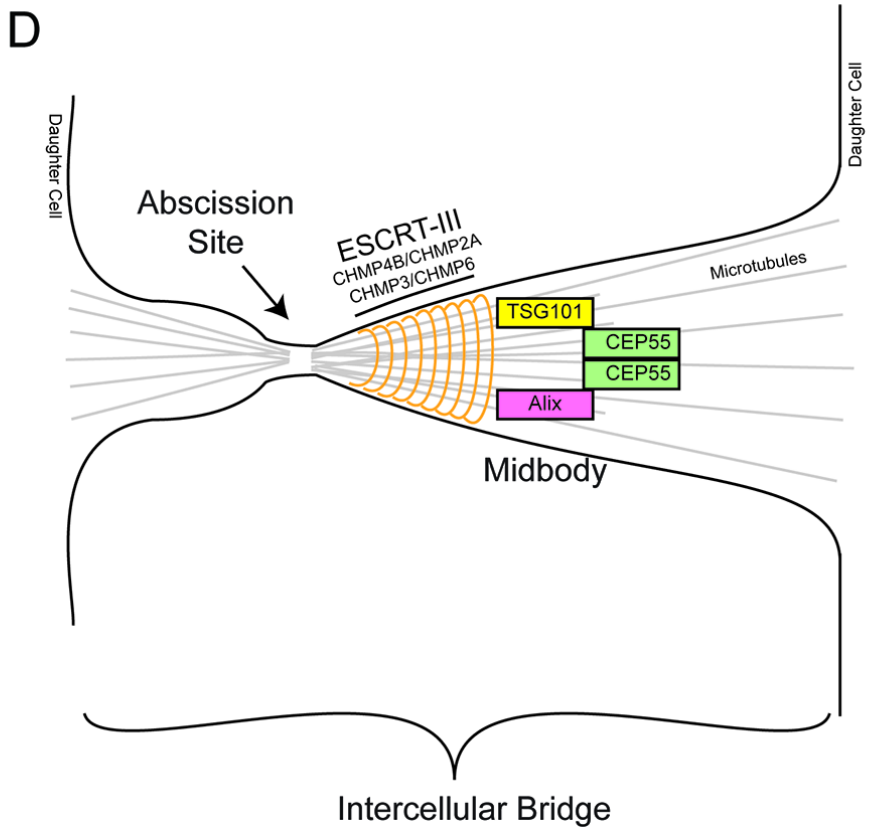
D
Daughter Cell
Daughter Cell
Abscission Site
ESCRT-III
CHMP4B/CHMP2A
CHMP3/CHMP6
Microtubules
TSG101
CEP55
CEP55
Alix
Midbody
Intercellular Bridge

A

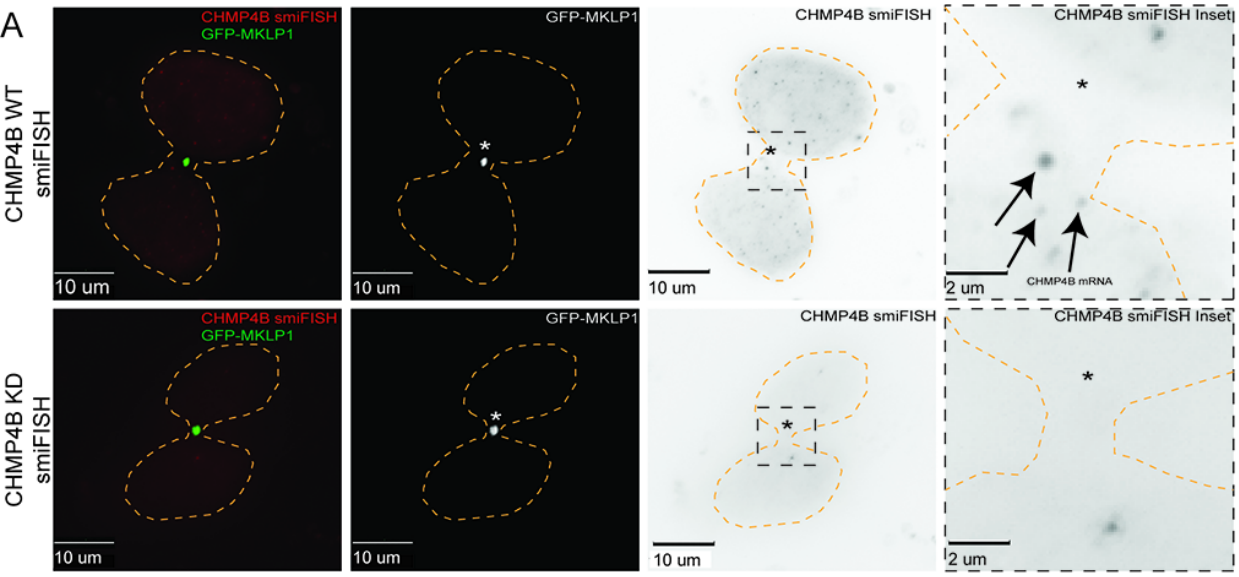

B

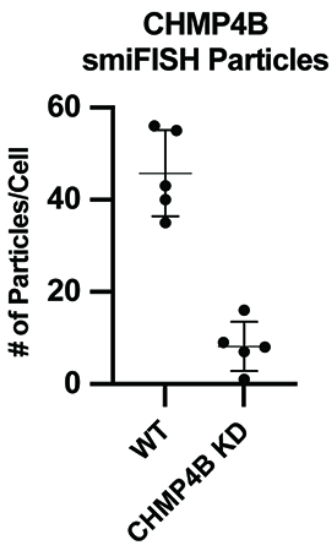

C

Ribosomal and initiation protein enrichment in the MB

Category	Data set	Enrichment Score	Citation
Ribosomal Proteins	Prekeris Lab	70.85	23
	Simpson Lab	54.95	24
	Echard Lab	80.71	8
Translation Initiation Factors	Prekeris Lab	49.07	23
	Simpson Lab	38.73	24
	Echard Lab	80.4	8

D

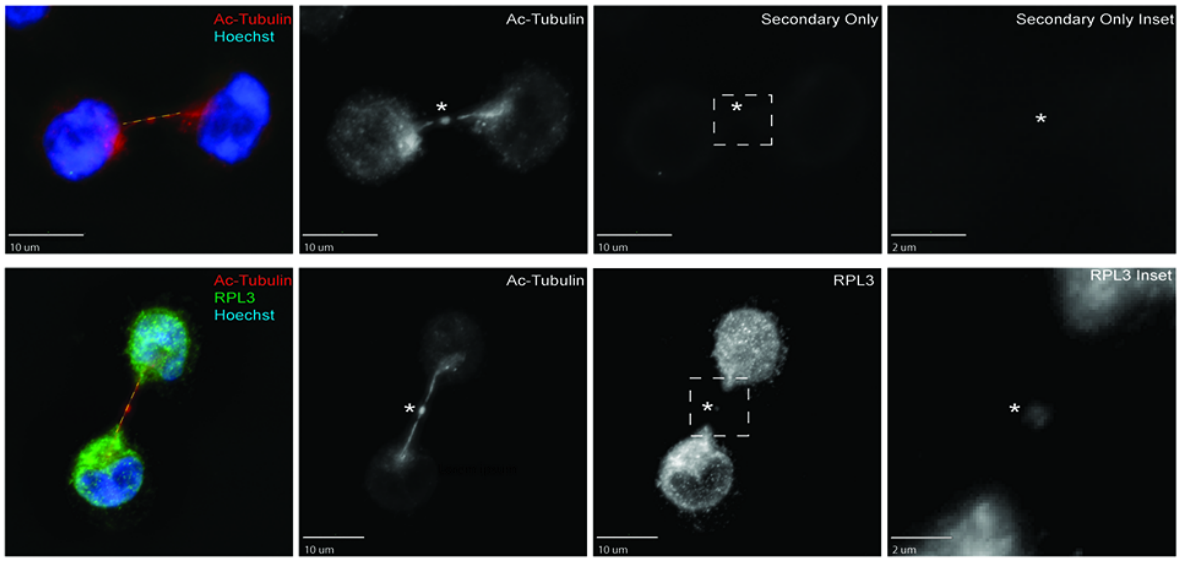

E

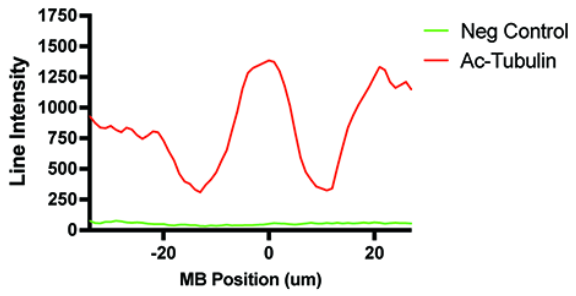

F

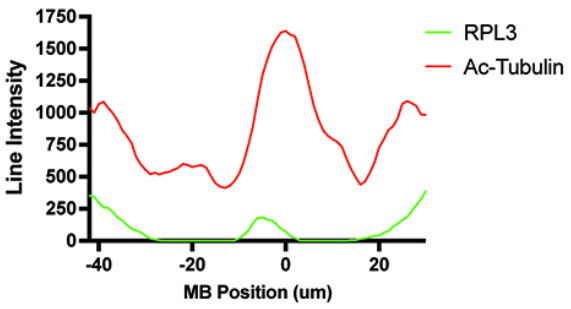

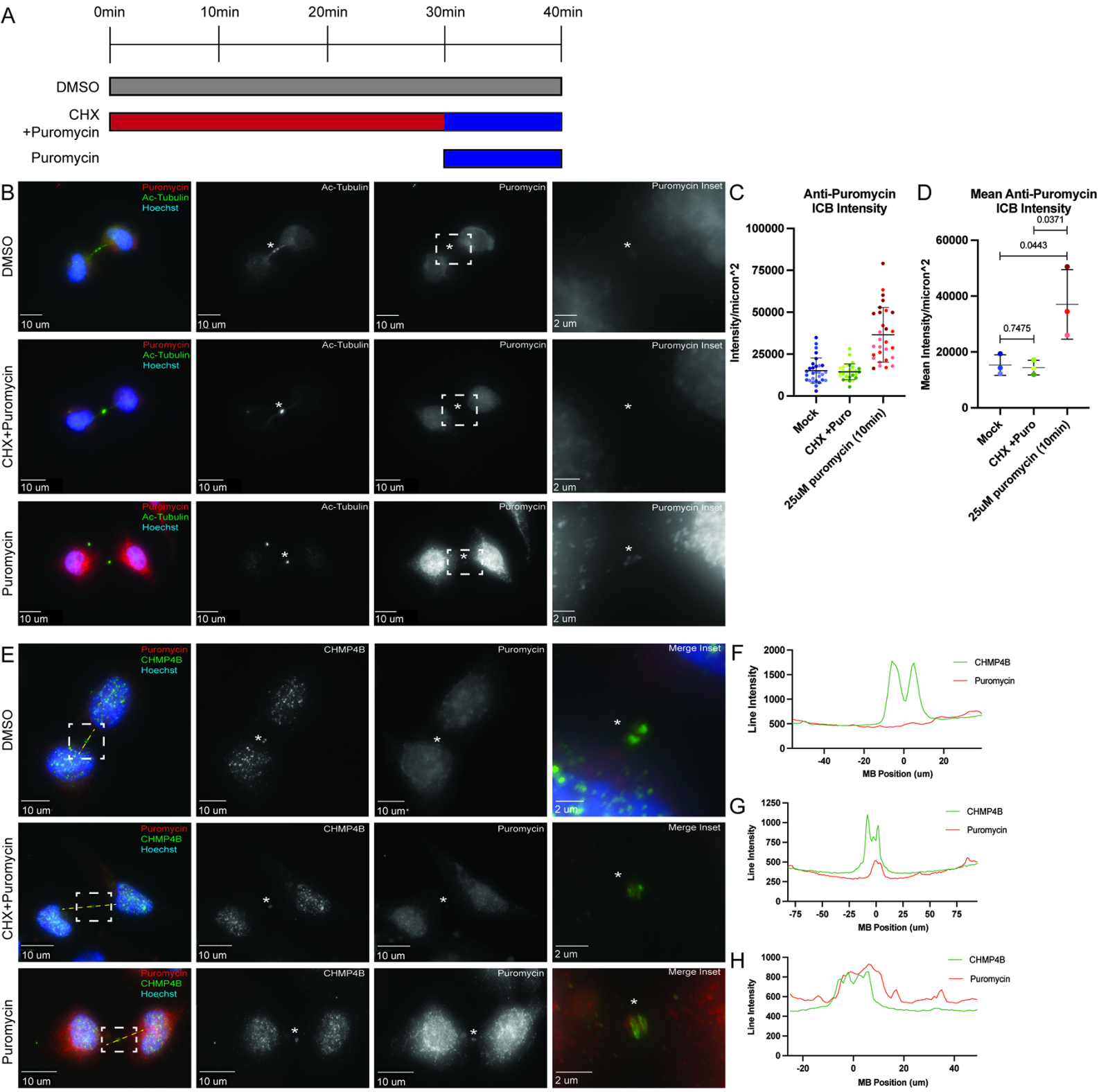
A
0min
10min
20min
30min
40min
DMSO
CHX +Puromycin
Puromycin
B
DMSO
CHX+Puromycin
Puromycin
Puromycin
Ac-Tubulin
Hoechst
Puromycin Inset
10 um
2 um
C
Anti-Puromycin ICB Intensity
Intensity/micron^2
100000
75000
50000
25000
0
Mock
CHX +Puro
25uM puromycin (10min)
D
Mean Anti-Puromycin ICB Intensity
Mean Intensity/micron^2
60000
40000
20000
0
0.0371
0.0443
0.7475
Mock
CHX +Puro
25uM puromycin (10min)
E
DMSO
CHX+Puromycin
Puromycin
Puromycin
CHMP4B
Hoechst
Merge Inset
10 um
2 um
F
Line Intensity
MB Position (um)
CHMP4B
Puromycin
G
Line Intensity
MB Position (um)
CHMP4B
Puromycin
H
Line Intensity
MB Position (um)
CHMP4B
Puromycin

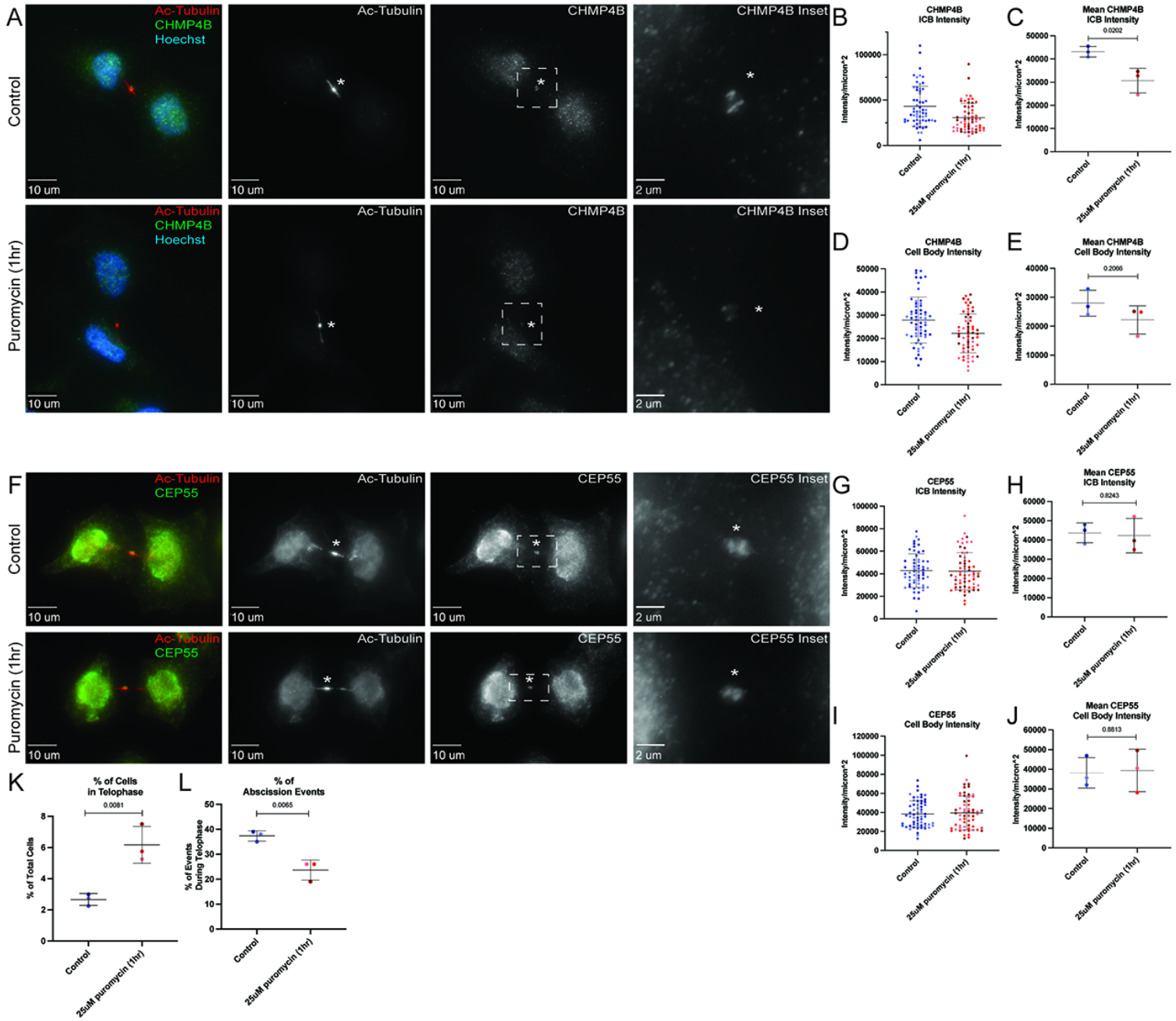
A
Ac-Tubulin
CHMP4B
Hoechst
Ac-Tubulin
CHMP4B
CHMP4B Inset
Control
Puromycin (1hr)
10 um
2 um
B
CHMP4B ICB Intensity
C
Mean CHMP4B ICB Intensity
0.0202
D
CHMP4B Cell Body Intensity
E
Mean CHMP4B Cell Body Intensity
0.2066
Intensity/micron^2
Control
25uM puromycin (1hr)
F
Ac-Tubulin
CEP55
CEP55 Inset
G
CEP55 ICB Intensity
H
Mean CEP55 ICB Intensity
0.8243
I
CEP55 Cell Body Intensity
J
Mean CEP55 Cell Body Intensity
0.8813
K
% of Cells in Telophase
0.0081
% of Total Cells
L
% of Abscission Events
0.0065
% of Events During Telophase

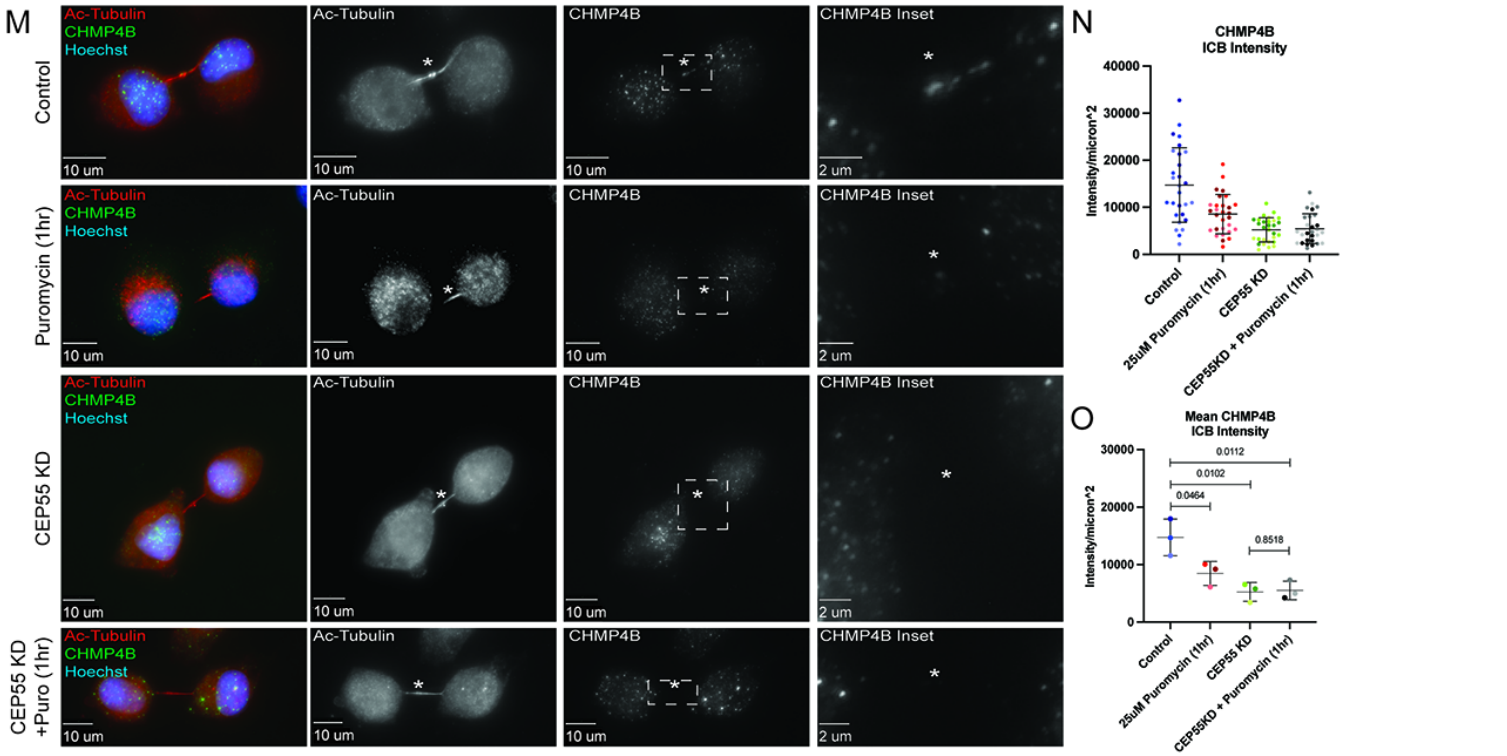
M
Ac-Tubulin
CHMP4B
Hoechst
Ac-Tubulin
CHMP4B
CHMP4B Inset
Control
Puromycin (1hr)
CEP55 KD
CEP55 KD +Puro (1hr)
10 um
2 um
N
CHMP4B ICB Intensity
Intensity/micron^2
Control
25uM Puromycin (1hr)
CEP55 KD
CEP55KD + Puromycin (1hr)
O
Mean CHMP4B ICB Intensity
0.0112
0.0102
0.0464
0.8518

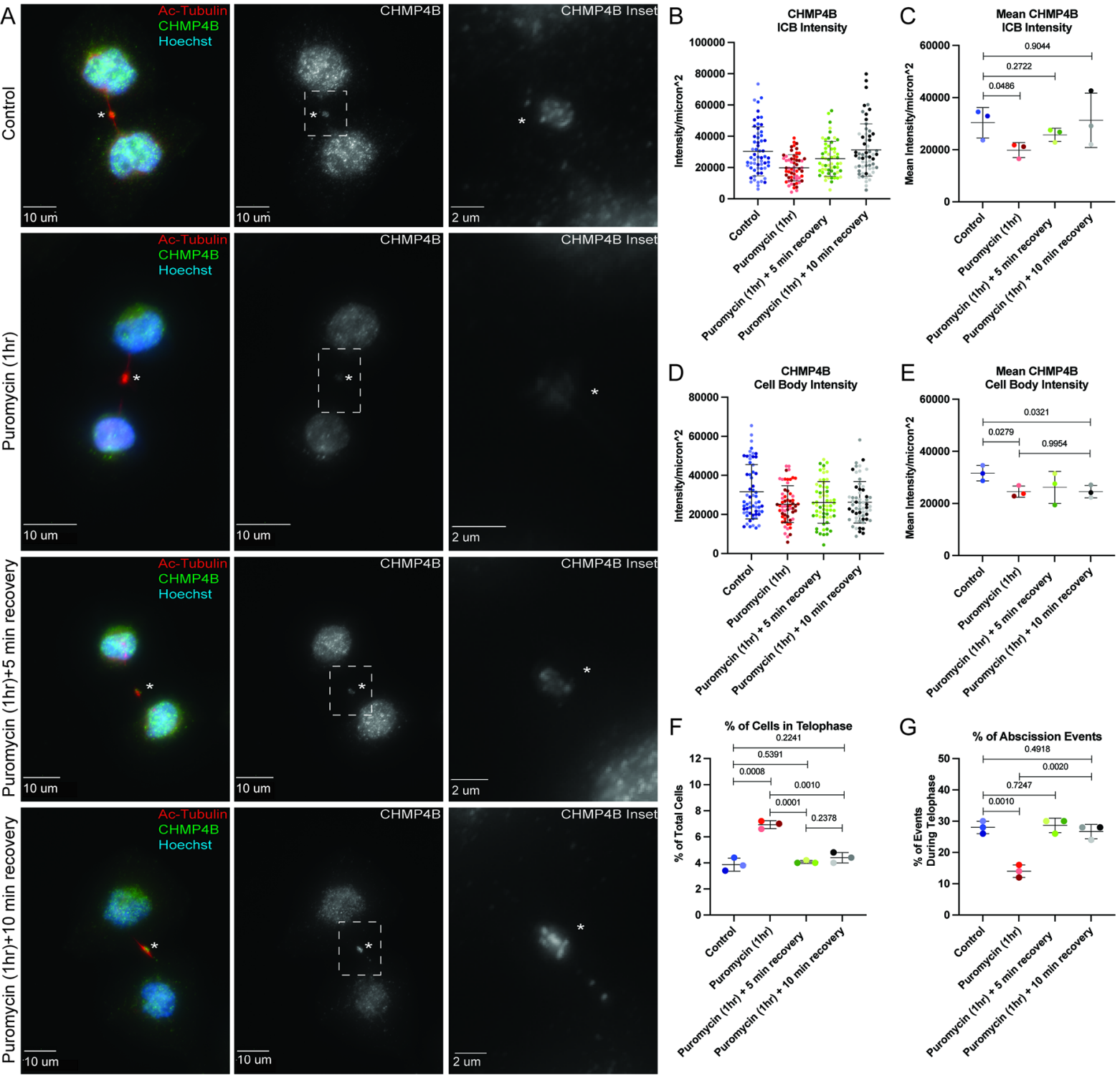
A
Control
Puromycin (1hr)
Puromycin (1hr)+5 min recovery
Puromycin (1hr)+10 min recovery
Ac-Tubulin
CHMP4B
Hoechst
CHMP4B
CHMP4B Inset
10 um
2 um
B
CHMP4B ICB Intensity
Intensity/micron^2
C
Mean CHMP4B ICB Intensity
Mean Intensity/micron^2
0.9044
0.2722
0.0486
D
CHMP4B Cell Body Intensity
E
Mean CHMP4B Cell Body Intensity
0.0321
0.0279
0.9954
F
% of Cells in Telophase
% of Total Cells
0.2241
0.5391
0.0008
0.0010
0.0001
0.2378
G
% of Abscission Events
% of Events During Telophase
0.4918
0.0020
0.7247
0.0010
Control
Puromycin (1hr)
Puromycin (1hr) + 5 min recovery
Puromycin (1hr) + 10 min recovery

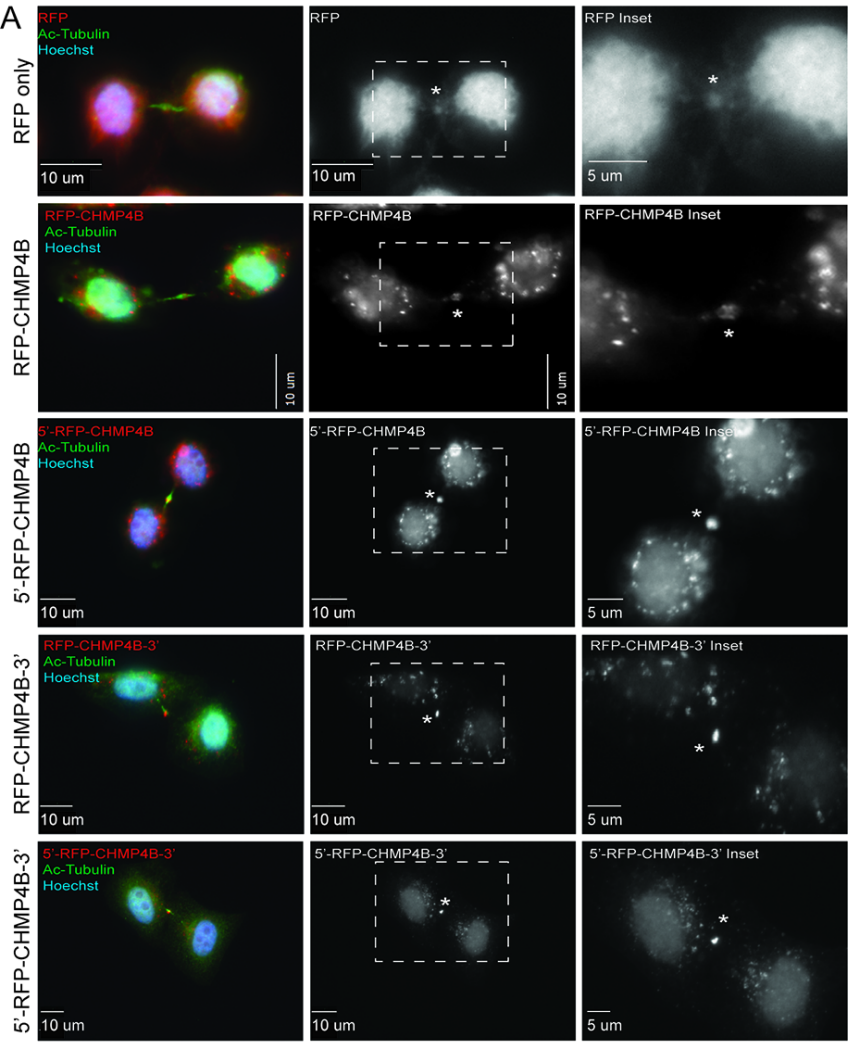
A
RFP only
RFP-CHMP4B
5'-RFP-CHMP4B
RFP-CHMP4B-3'
5'-RFP-CHMP4B-3'
RFP
Ac-Tubulin
Hoechst
RFP Inset
RFP-CHMP4B
RFP-CHMP4B Inset
5'-RFP-CHMP4B
5'-RFP-CHMP4B Inset
RFP-CHMP4B-3'
RFP-CHMP4B-3' Inset
5'-RFP-CHMP4B-3'
5'-RFP-CHMP4B-3' Inset
10 um
5 um

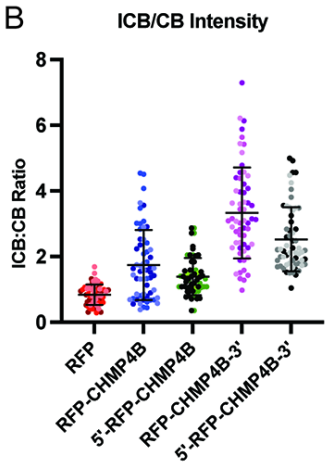
B
ICB/CB Intensity
ICB:CB Ratio
RFP
RFP-CHMP4B
5'-RFP-CHMP4B
RFP-CHMP4B-3'
5'-RFP-CHMP4B-3'

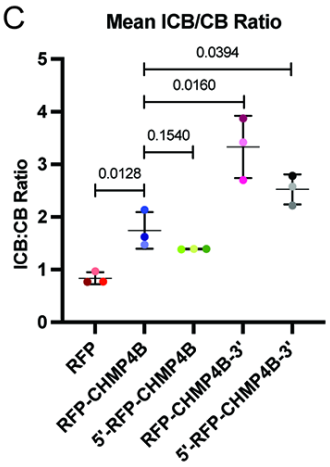
C
Mean ICB/CB Ratio
ICB:CB Ratio
0.0394
0.0160
0.1540
0.0128
RFP
RFP-CHMP4B
5'-RFP-CHMP4B
RFP-CHMP4B-3'
5'-RFP-CHMP4B-3'

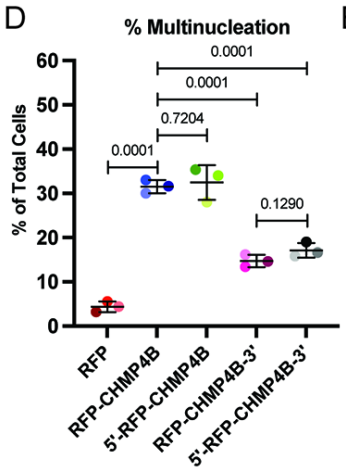
D
% Multinucleation
% of Total Cells
0.0001
0.0001
0.7204
0.0001
0.1290
RFP
RFP-CHMP4B
5'-RFP-CHMP4B
RFP-CHMP4B-3'
5'-RFP-CHMP4B-3'

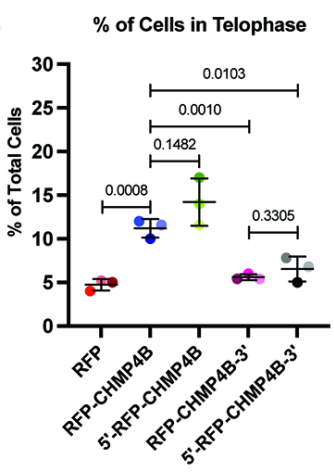
E
% of Cells in Telophase
% of Total Cells
0.0103
0.0010
0.1482
0.0008
0.3305
RFP
RFP-CHMP4B
5'-RFP-CHMP4B
RFP-CHMP4B-3'
5'-RFP-CHMP4B-3'

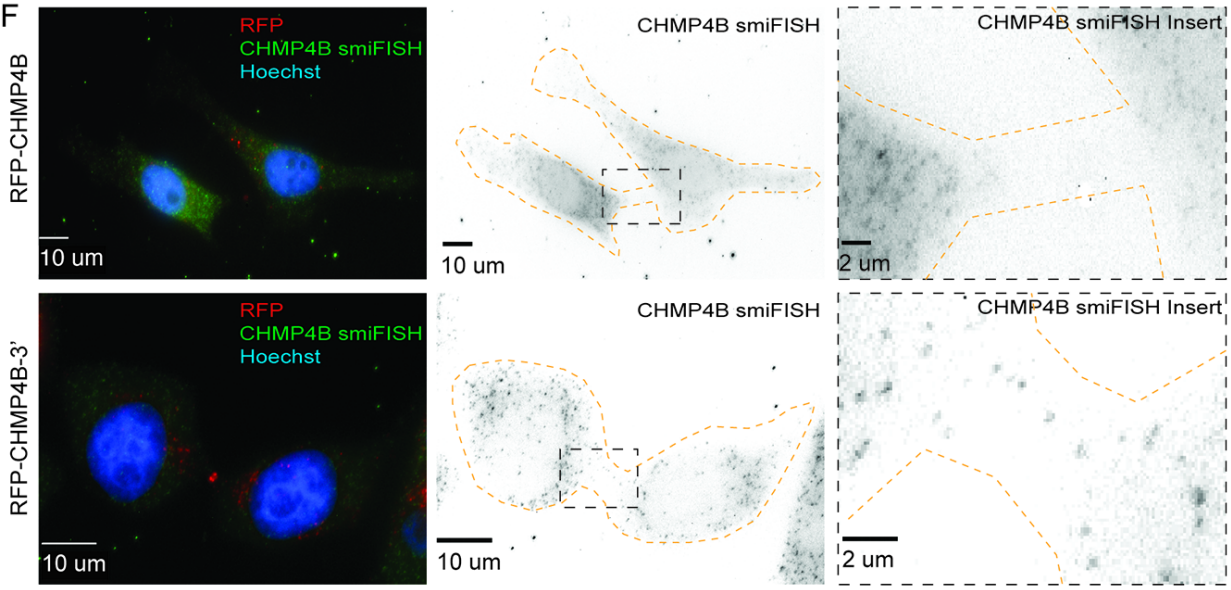
F
RFP-CHMP4B
RFP-CHMP4B-3'
RFP
CHMP4B smiFISH
Hoechst
CHMP4B smiFISH
CHMP4B smiFISH Insert
10 um
2 um

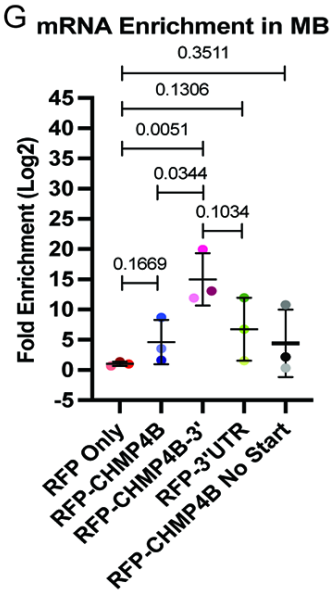
G
mRNA Enrichment in MB
Fold Enrichment (Log2)
0.3511
0.1306
0.0051
0.0344
0.1034
0.1669
RFP Only
RFP-CHMP4B
RFP-CHMP4B-3'
RFP-3'UTR
RFP-CHMP4B No Start

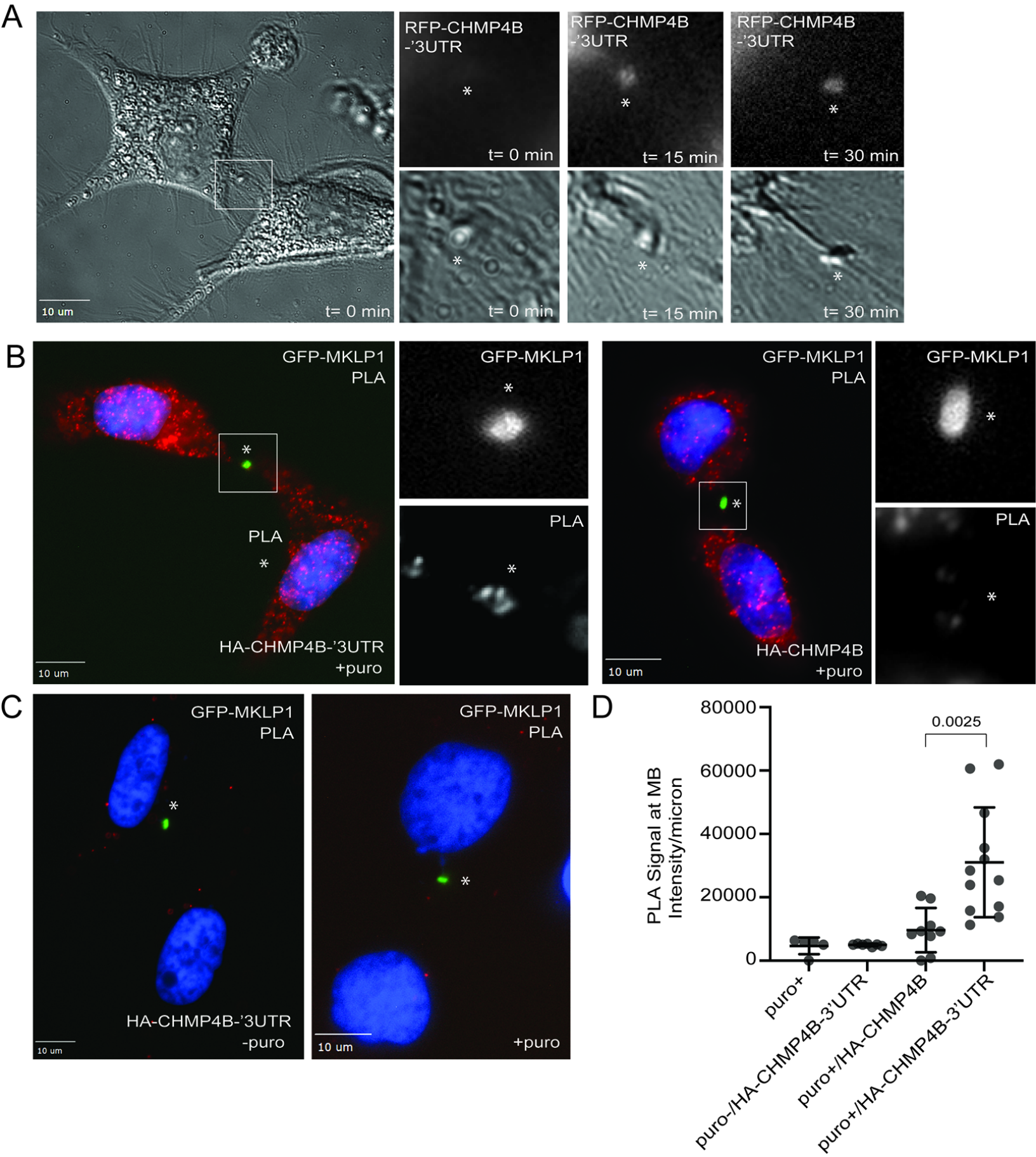
A
RFP-CHMP4B
-'3UTR
t= 0 min
t= 15 min
t= 30 min
10 um
B
GFP-MKLP1
PLA
HA-CHMP4B-'3UTR
+puro
HA-CHMP4B
C
-puro
D
PLA Signal at MB
Intensity/micron
80000
60000
40000
20000
0
0.0025
puro+
puro-/HA-CHMP4B-3'UTR
puro+/HA-CHMP4B
puro+/HA-CHMP4B-3'UTR

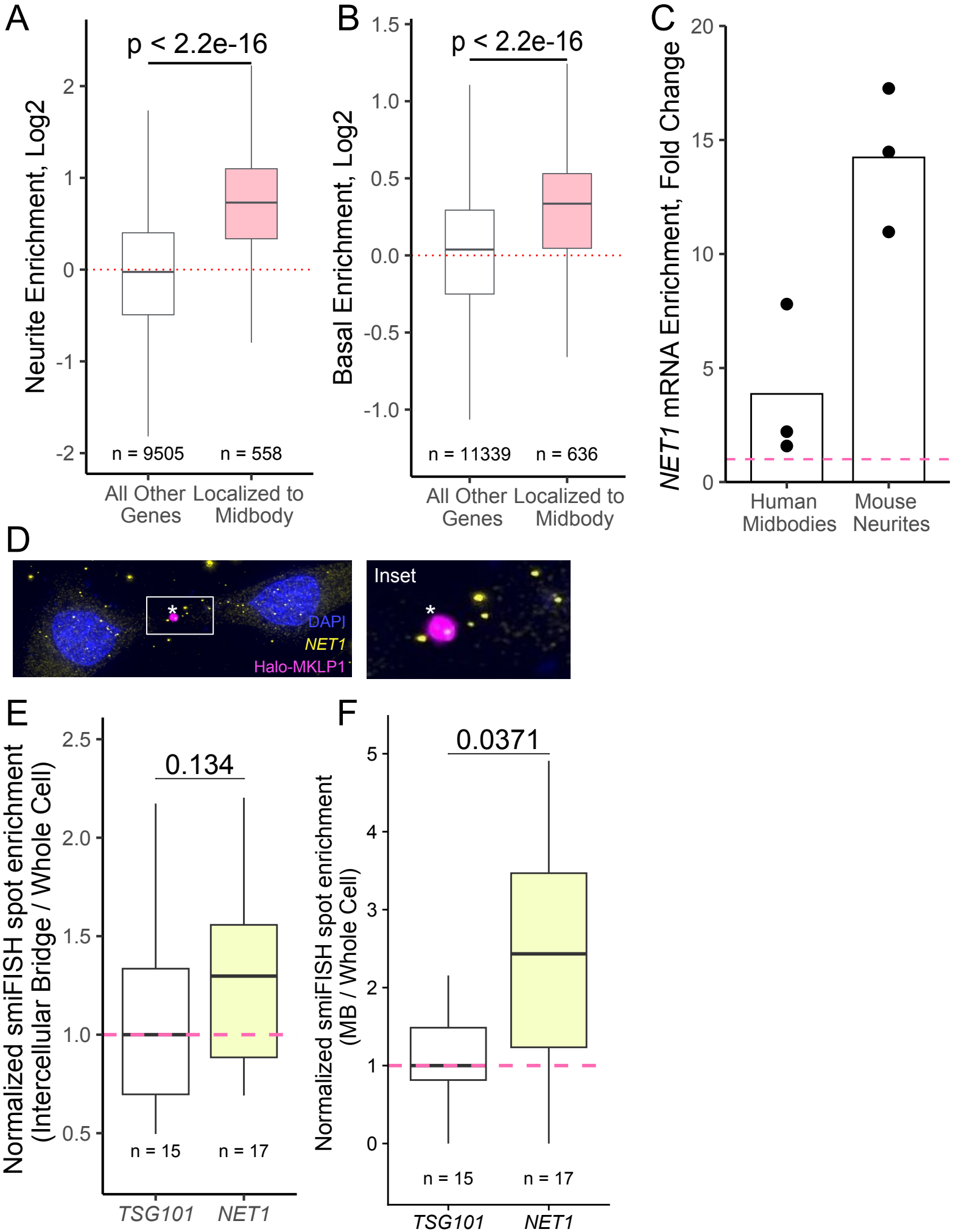
A
p < 2.2e-16
Neurite Enrichment, Log2
2
1
0
-1
-2
n = 9505
n = 558
All Other Genes
Localized to Midbody
B
p < 2.2e-16
Basal Enrichment, Log2
1.5
1.0
0.5
0.0
-0.5
-1.0
n = 11339
n = 636
All Other Genes
Localized to Midbody
C
NET1 mRNA Enrichment, Fold Change
20
15
10
5
0
Human Midbodies
Mouse Neurites
D
DAPI
NET1
Halo-MKLP1
Inset
E
0.134
Normalized smiFISH spot enrichment (Intercellular Bridge / Whole Cell)
2.5
2.0
1.5
1.0
0.5
n = 15
n = 17
TSG101
NET1
F
0.0371
Normalized smiFISH spot enrichment (MB / Whole Cell)
5
4
3
2
1
0
n = 15
n = 17
TSG101
NET1

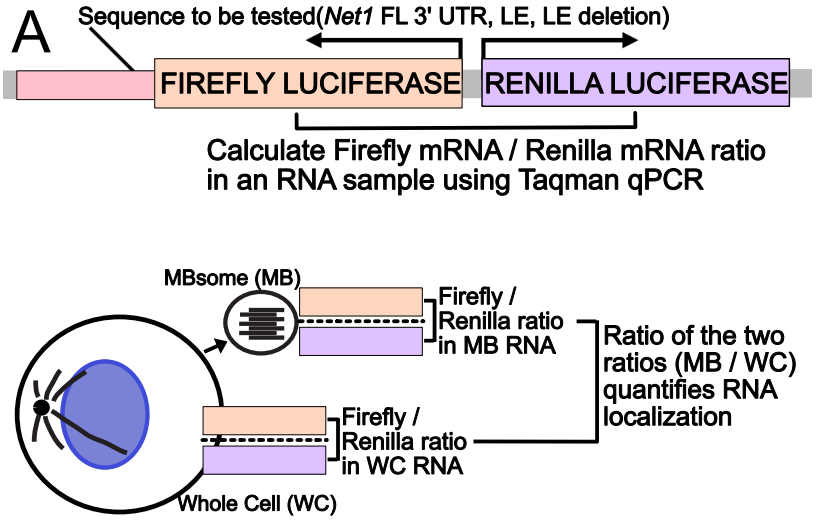
A
Sequence to be tested(Net1 FL 3' UTR, LE, LE deletion)
FIREFLY LUCIFERASE
RENILLA LUCIFERASE
Calculate Firefly mRNA / Renilla mRNA ratio in an RNA sample using Taqman qPCR
MBsome (MB)
Firefly / Renilla ratio in MB RNA
Ratio of the two ratios (MB / WC) quantifies RNA localization
Firefly / Renilla ratio in WC RNA
Whole Cell (WC)

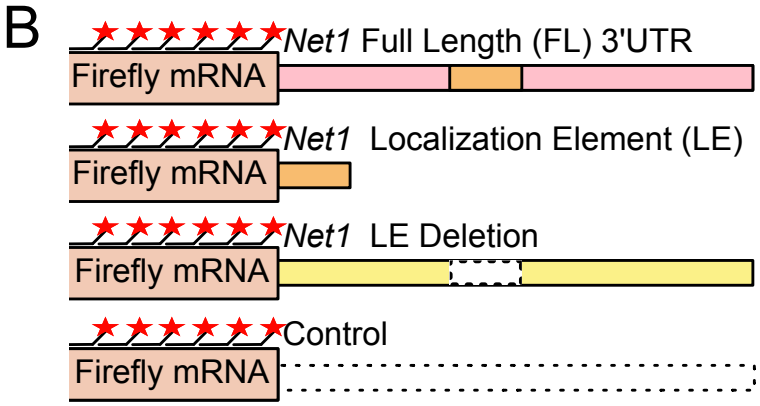
B
Net1 Full Length (FL) 3'UTR
Firefly mRNA
Net1 Localization Element (LE)
Firefly mRNA
Net1 LE Deletion
Firefly mRNA
Control
Firefly mRNA

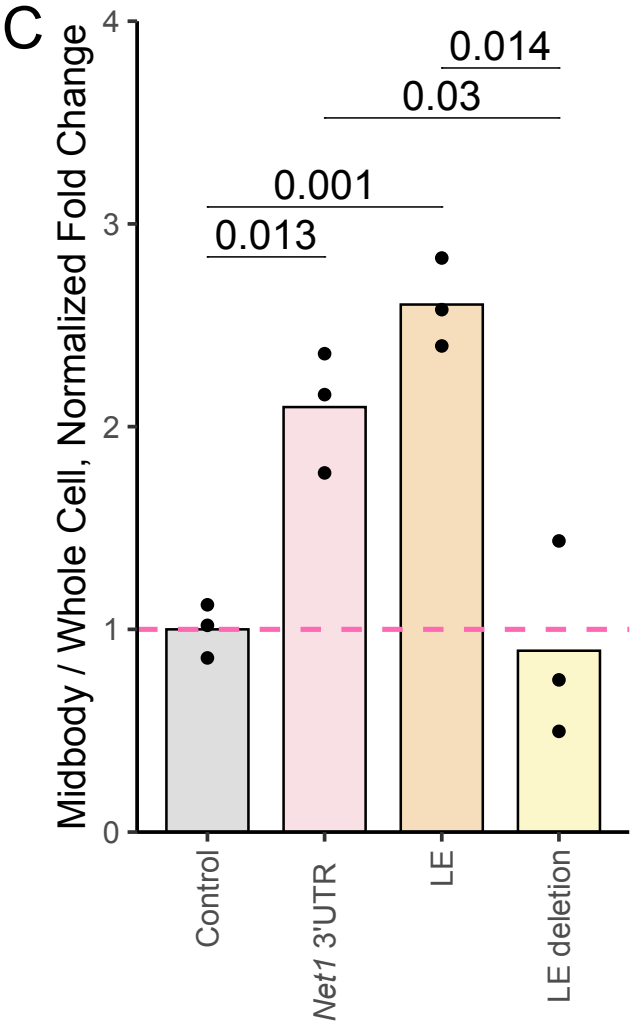
C
Midbody / Whole Cell, Normalized Fold Change
0
1
2
3
4
0.014
0.03
0.001
0.013
Control
Net1 3'UTR
LE
LE deletion

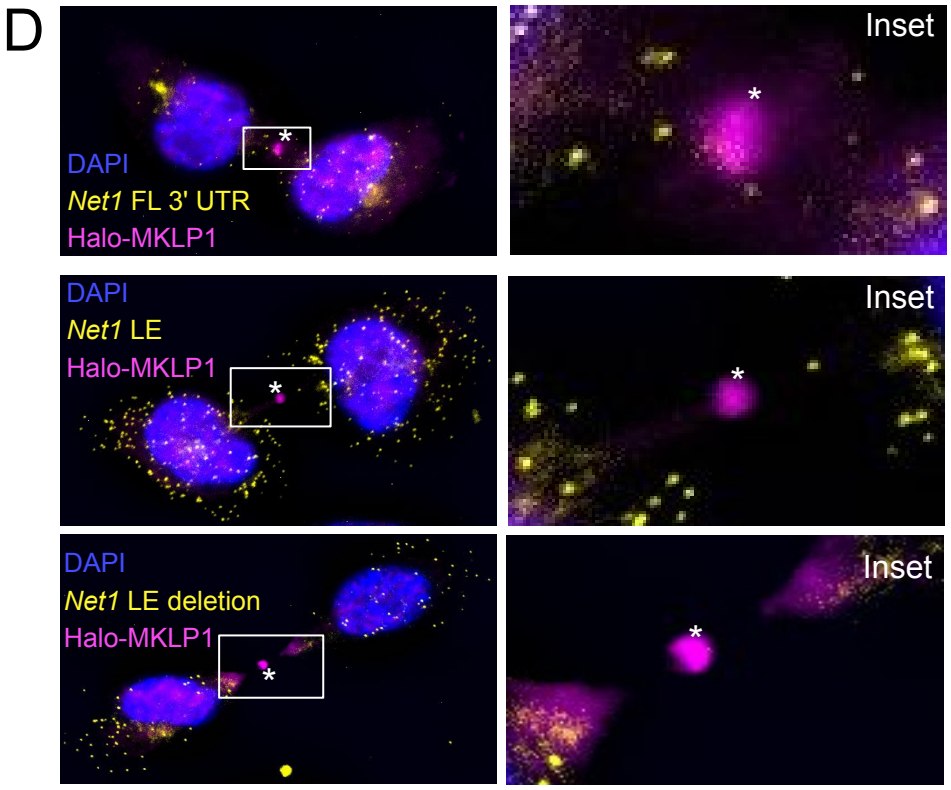
D
DAPI
Net1 FL 3' UTR
Halo-MKLP1
Inset
DAPI
Net1 LE
Halo-MKLP1
Inset
DAPI
Net1 LE deletion
Halo-MKLP1
Inset

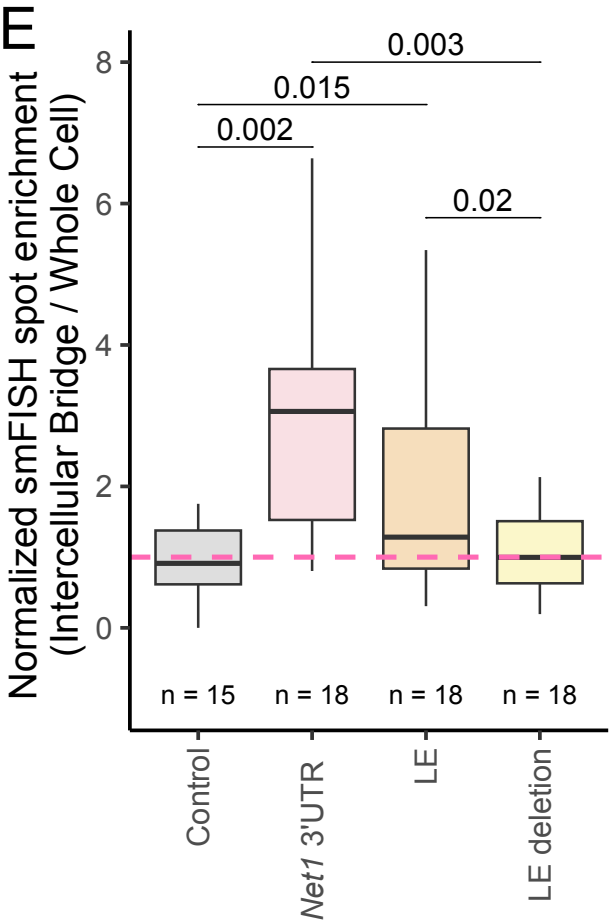
E
Normalized smFISH spot enrichment (Intercellular Bridge / Whole Cell)
0
2
4
6
8
0.003
0.015
0.002
0.02
n = 15
n = 18
n = 18
n = 18
Control
Net1 3'UTR
LE
LE deletion